Jacobian-based natural frequency analysis of parallel manipulators

Hoevenaars, A. G.L.; Krut, S.; Herder, J. L.

DOI
10.1016/j.mechmachtheory.2019.103775

Publication date
2020

Document Version
Accepted author manuscript

Published in
Mechanism and Machine Theory

Jacobian-based natural frequency analysis of parallel manipulators

A.G.L. Hoevenaars[a], S. Krut[b], J.L. Herder[a]

[a] *Faculty of Mechanical, Maritime and Materials Engineering, Delft University of Technology, 2628 CD Delft, The Netherlands*
[b] *Laboratoire d'Informatique, de Robotique et de Microélectronique de Montpellier, 161 Rue Ada, 34090 Montpellier, France*

Abstract

The dynamic performance of a parallel manipulator is often limited by its natural frequencies. These frequencies are a result of the controlled actuator stiffness and the mechanical design. Typically, only the lowest natural frequencies are of interest. However, existing methods to analyze natural frequencies of parallel manipulators with flexible links have been developed in a high-dimensional generalized coordinate space. This paper presents a novel natural frequency analysis method for parallel manipulators that focuses on the lowest natural frequencies and which expresses the corresponding eigenmodes in the end-effector Cartesian reference frame. The analysis method combines a flexible-body stiffness analysis method with a rigid-body inertia analysis method. As an example, the two lowest natural frequencies of the Heli4 robot are modeled and measured over a range of controlled actuator stiffness values for a single pose. The results show that structural compliance in the mechanical parts of the Heli4 robot is significant for actuator stiffness values above roughly 1000 Nm/rad. For an actuator stiffness value of 4000 Nm/rad, consideration of the structural compliance reduces the maximum prediction error for the two lowest natural frequencies from 33% to 6%.

Keywords: parallel manipulator, natural frequencies, eigenmodes, stiffness, inertia, screw theory

*Corresponding author
Email addresses: teunhoevenaars@gmail.com (A.G.L. Hoevenaars), sebastien.krut@lirmm.fr (S. Krut), j.l.herder@tudelft.nl (J.L. Herder)

1. Introduction

Applications that require manipulators with a high dynamic performance often use parallel manipulators because of their favorable stiffness-over-inertia ratio, i.e. higher natural frequencies. Higher natural frequencies increase the controllable position bandwidth, which explains the popularity of parallel robots in pick-and-place applications [1, 2, 3, 4]. Another application is telemanipulation, for which high-bandwidth force feedback haptic master devices are developed, such as those introduced by Birglen et al. [5] and Lambert and Herder [6]. Therefore, an important performance indicator of parallel manipulators is the set of lowest natural frequencies, because they are a direct indication of the controllable bandwidth.

To calculate the natural frequencies, stiffness and inertia matrices need to be developed [7, 8]. Stiffness and inertia matrices are a direct consequence of mechatronic design choices, and are a function of the location in the workspace [9]. For a fast and effective search of the design space of a parallel manipulator, closed-form expressions for the stiffness and inertia models are desired. One approach to develop such models is through polynomial fitting, as for example done by Carbonari [10]. A disadvantage of this method is that it can only be applied after a manipulator has already been realized.

An alternative approach is to use Jacobian-based modeling methods, which rely on linearization of the dynamics around the instantaneous pose of the robot. As discussed above, a key performance indicator of a robot's dynamics are its natural frequencies. In order to perform a natural frequency analysis, a stiffness model and an inertia model must be developed in the same coordinate space.

Various researchers have obtained Jacobian-based stiffness and inertia matrices in Cartesian space. Gosselin developed an expression for the stiffness matrix in Cartesian space using a Jacobian mapping of stiffness values from joint space to Cartesian space [11]. Bhattacharya et al. [12] and Khalil and Ibrahim [13] developed general inertia analysis methods, while Lebret et al. [14] developed an inertia analysis method specifically for the Stewart-Gough platform and Callegari [15] specifically for a 3-RCC parallel manipulator. In each of these works, matrices are initially formulated in a generalized coordinate space, and subsequently mapped to Cartesian end-effector space. Also, they are all based on the assumption of rigid body motion.

The assumption of rigid body motion does not always hold, as observed among others by Lian et al. [16] and Vivas et al. [17]. In order to consider

structural compliance of the links, the dimension of Jacobian-based models must be extended. Stiffness models that consider structural compliance mostly rely on the incorporation of Euler-Bernoulli beam models. These flexible-body models add additional sets of generalized coordinates to the ones required to describe the rigid body motions. Many examples exist of stiffness analysis methods in which structural compliance is considered in extended sets of generalized coordinates [18, 19, 20, 21, 22].

If a flexible-body stiffness analysis is combined with an inertia analysis, an elastodynamic model is formed. To develop such an elastodynamic model, different approaches can be taken. For example, the Matrix Structural Analysis [23], Lagrange's equations [24, 25], or recursive methods [26, 27] have been used. Manipulator-specific analyses have also been performed [28, 22].

This paper focuses on the use of Jacobian matrices to express equations in an extended set of generalized coordinates, which is often referred to as the Virtual Joint Method. In this context, Alessandro and Rosario [29], Bouzgarrou et al. [30], and Germain et al. [7] all extended inertia matrices to the set of generalized coordinates that were also used in the stiffness analyses. A similar approach was taken by Briot et al. [31], but as an extra step they also mapped the resulting extended stiffness and inertia matrices to Cartesian end-effector space for more efficient and insightful natural frequency analysis. Chen et al. [32] focused on link curvature caused by link compliance, and combined their resulting stiffness analysis with an inertia analysis to analyze the set of lowest natural frequencies at various end-effector poses. Despite their differences, these methods do have one thing in common: they all match the dimension of the inertia matrix with that of the extended stiffness matrix, thereby including both the elastic energy as well as the kinetic energy of all deforming bodies in the analysis. This makes inertia analysis significantly more complex.

However, elastic energy and kinetic energy are two different concepts and the elastic model and the kinetic model do not necessarily have to be developed with the same level of detail. Such separation of elastic model and kinetic model is beneficial if, for example, the elastic energy exchanged by deforming bodies is significant, but the kinetic energy involved in the elastically deforming bodies is negligible. For a natural frequency analysis, the only requirement on the resulting stiffness and inertia matrices is that they are expressed in the same coordinate spaces. Generally, the motion of interest is that of the end-effector with respect to the base, and therefore the Cartesian end-effector space is a logical choice.

This paper aims to develop a method to analyze the natural frequencies of a general parallel manipulator with flexible links without the need for flexible-body inertia analysis. For that, the dimensions of the elastic- and the inertia models are decoupled. The decoupling of model dimensions is realized by developing both models in their own set of generalized coordinates, and subsequently mapping the resulting matrices onto a single Cartesian end-effector space using Jacobian matrices. For that purpose, a Cartesian stiffness analysis method will be combined with a novel expression for the Cartesian inertia matrix of a parallel manipulator. This novel expression will make use of Jacobian analysis techniques based on screw theory.

The structure of this paper is as follows. First, in the Method section the novel Cartesian inertia analysis method is derived, and the requirements on the Cartesian stiffness matrix analysis are discussed. It is then described how these analyses can be combined to perform a natural frequency analysis, and an example analysis will be performed for the Heli4 robot. For the example, the two lowest natural frequencies will be analyzed in one pose as a function of variable actuator stiffness. Finally, these natural frequencies will be verified with experiments.

2. Jacobian-Based Natural Frequency Analysis Method

The central idea of this paper is to develop a method to analyze only those eigenmodes that involve the complete multibody system, and ignore eigenmodes of individual legs and individual links. Because the motion vector of a body can be described by a twist, these eigenmodes will be referred to as *eigentwists*.

If it is assumed that the total energy of a parallel manipulator consists only of kinetic energy and elastic energy, then the Lagrangian can be written as

$$\mathcal{L} = \frac{1}{2}\left(\$_{t,e}^{\top}\mathbf{M}\$_{t,e} - \$_{d,e}^{\top}\mathbf{K}\$_{d,e}\right) \tag{1}$$

where $\mathbf{M}$ is the 6×6 Cartesian mass matrix and $\mathbf{K}$ is the 6×6 Cartesian stiffness matrix. For a general parallel manipulator, $\$_{t,e}$ is the twist of the end-effector, and $\$_{d,e}$ is the displacement twist of the end-effector from its equilibrium pose, which can be expressed as

$$\$_{t,e} = \begin{bmatrix}\dot{\boldsymbol{\phi}} \\ \dot{\mathbf{p}}\end{bmatrix} \qquad \$_{d,e} = \begin{bmatrix}d\boldsymbol{\phi} \\ d\mathbf{p}\end{bmatrix} \tag{2}$$

where $\dot{\boldsymbol{\phi}}$ is the angular velocity of the end-effector, $\dot{\mathbf{p}}$ its linear velocity, $d\boldsymbol{\phi}$ the differential angular displacement of the end-effector from its neutral pose, and $d\mathbf{p}$ the differential linear displacement from that pose. As such, for small displacements,

$$\$_{t,e} = \dot{\$}_{d,e} \tag{3}$$

and therefore Eq. (1) can be rewritten as

$$\mathcal{L} = \frac{1}{2}\left(\dot{\$}_{d,e}^{\top}\mathbf{M}\dot{\$}_{d,e} - \$_{d,e}^{\top}\mathbf{K}\$_{d,e}\right) \tag{4}$$

If the net external wrench applied on the end-effector is zero, and all velocity-dependent terms are assumed negligible, then the Euler-Lagrange equation reads

$$\frac{d}{dt}\left(\frac{\delta\mathcal{L}}{\delta\dot{\$}_{d,e}}\right) - \frac{\delta\mathcal{L}}{\delta\$_{d,e}} = \mathbf{M}\ddot{\$}_{d,e} + \mathbf{K}\$_{d,e} = \mathbf{0} \tag{5}$$

and the solution to Eq. (5) satisfies

$$\left(\omega_i^2\mathbf{M} - \mathbf{K}\right)\$_{v,i} = \mathbf{0} \qquad \text{for } i = 1, 2, ..., 6. \tag{6}$$

where ω_i is the ith natural frequencies in rad/s and $\$_{v,i}$ is the corresponding eigentwist. The natural frequencies of the system can be obtained from

$$\det\left(\omega_i^2\mathbf{M} - \mathbf{K}\right) = 0 \qquad \text{for } i = 1, 2, ..., 6 \tag{7}$$

and the eigentwist $\$_{v,i}$ corresponding to ω_i can be calculated from the set of linear equations that result from inserting solution ω_i into Eq. (6).

2.1. Novel Jacobian-Based Inertia Analysis Method

In this section a novel Jacobian-based inertia analysis method is developed, so that the natural frequencies can be analyzed in Cartesian space. The novelty of this method is in the use of inverse and forward Jacobian matrices to map a given end-effector twist on the corresponding twist for each individual body of a parallel manipulator. As such, this analysis assumes only rigid body motion.

In a multibody system, the total kinetic energy is the sum of the kinetic energies of the individual bodies. For a parallel manipulator with N legs this translates into

$$\mathcal{T} = \sum_{i=1}^{N}\sum_{j=1}^{J_i-1}\frac{1}{2}\$_{t,i,j}^{\top}\mathbf{M}_{i,j}\$_{t,i,j} + \frac{1}{2}\$_{t,e}^{\top}\mathbf{M}_e\$_{t,e} \tag{8}$$

where J_i is the number of joints in the ith leg, $\$_{t,i,j}$ is the twist of the body following the jth joint of leg i, and $\mathbf{M}_{i,j}$ is the 6×6 mass matrix of this body, expressed in the same reference frame as the twists. For each leg the last body, $j = J_i$, is excluded from the summation in Eq. (8) because for each leg this body is the end-effector. Instead, to prevent the inertia of the end-effector, $\mathbf{M}_e$, to be counted N times, it is added as a separate term.

The difficulty for a parallel manipulator is to determine the twists of the different bodies in each leg, i.e. each $\$_{t,i,j}$ in Eq. (8). This is achieved by making use of inverse and forward Jacobian mappings that can be derived for each leg. The inverse Jacobian of a leg maps $\$_{t,e}$ on all joint velocities of that leg, which are collected in the vector $\dot{\mathbf{q}}_i$ for the considered leg i, each element of which is associated to a unit twist. Then, for each body in the considered leg the contributing twists can be added to obtain the twist of that body as a function of the end-effector twist:

$$\$_{t,i,j} = \mathbf{J}_{i,j}\mathbf{J}_i^{-1}\$_{t,e}. \tag{9}$$

where $\mathbf{J}_i^{-1}$ is the inverse Jacobian for the ith leg, which maps $\$_{t,e}$ onto $\dot{\mathbf{q}}_i$, as developed in Ref. [33], and $\mathbf{J}_{i,j}$ is the forward Jacobian which contains the first j number of unit twists of leg i, complemented with a set of $(6-j)$ zero twists. Combination of Eq. (8) and Eq. (9) leads to

$$\mathcal{T} = \sum_{i=1}^{N}\sum_{j=1}^{J_i-1} \frac{1}{2}\$_{t,e}^{\top}\mathbf{J}_i^{-\top}\mathbf{J}_{i,j}^{\top}\mathbf{M}_{i,j}\mathbf{J}_{i,j}\mathbf{J}_i^{-1}\$_{t,e} + \frac{1}{2}\$_{t,e}^{\top}\mathbf{M}_e\$_{t,e} \tag{10}$$

where the mass matrices $\mathbf{M}_{i,j}$ and $\mathbf{M}_e$ must be expressed in the same Cartesian reference frame as in which all twists and wrenches are expressed.

Because $\$_{t,e}$ in Eq. (10) does not depend on the indices i and j of the summations, Eq. (10) can also be expressed as

$$\mathcal{T} = \frac{1}{2}\$_{t,e}^{\top}\left(\sum_{i=1}^{N}\sum_{j=1}^{J_i-1}\mathbf{J}_i^{-\top}\mathbf{J}_{i,j}^{\top}\mathbf{M}_{i,j}\mathbf{J}_{i,j}\mathbf{J}_i^{-1} + \mathbf{M}_e\right)\$_{t,e} \tag{11}$$

A comparison with the term that represent the kinetic energy in Eq. (4) shows that

$$\mathbf{M} = \sum_{i=1}^{N}\sum_{j=1}^{J_i-1}\mathbf{J}_i^{-\top}\mathbf{J}_{i,j}^{\top}\mathbf{M}_{i,j}\mathbf{J}_{i,j}\mathbf{J}_i^{-1} + \mathbf{M}_e \tag{12}$$

Since mass matrices are in general 6×6 full-rank matrices, the resulting matrix $\mathbf{M}$ will be as well.

2.2. Full-Rank Stiffness Matrix

In order to solve Eq. (7), both matrices $\mathbf{M}$ and $\mathbf{K}$ must be expressed in the same coordinate space. Since Eq. (12) expressed matrix $\mathbf{M}$ in a Cartesian reference frame. As such, matrix $\mathbf{K}$ may be expressed using any method as long as it produces a full rank Cartesian stiffness matrix.

To develop a full-rank stiffness matrix for limited-DoF manipulators [34], where the end-effector is constrained to less than 6 Degrees of Freedom (DoFs), structural stiffness of the constraining legs must be taken into account. As discussed in the Introduction section, various methods have been developed to include structural stiffness of the legs, and any of these methods can be used in tandem with the inertia analysis developed in Section 2.1. After all, elastic energy and kinetic energy are two different concepts and therefore the stiffness matrix and the inertia matrix do not necessarily have to be developed with the same level of detail, as long as the resulting matrices are expressed in the same coordinate frame.

In this paper, the Jacobian-based stiffness analysis method presented by Hoevenaars et al. [20] is used to obtain the 6×6 Cartesian stiffness matrix $\mathbf{K}$ of a parallel manipulator with flexible links. The general expression of this flexible-body stiffness matrix $\mathbf{K}_F$ is

$$\mathbf{K}_F = \left(-\frac{\partial \mathbf{J}_e^{-\top}}{\partial \mathbf{q}} \boldsymbol{\tau}_e \right) \mathbf{J}^{-1} + \mathbf{J}_e^{-\top} \mathbf{K}_{q,e} \mathbf{J}_e^{-1} \tag{13}$$

where for a general parallel manipulator with N non-redundant legs, $\mathbf{q}$ is the $6N \times 1$ vector containing all joint coordinates, in which virtual joint coordinates represent constrained directions in joint space, $\boldsymbol{\tau}_e$ is the joint torque vector where all zero entries associated to zero stiffness joints were removed, and $\mathbf{J}^{-1}$ is the $6N \times 6$ full inverse Jacobian as developed by Huang et al. [33]. The matrix $\mathbf{J}_e^{-1}$ is the inverse Jacobian of elasticity, which corresponds to the matrix $\mathbf{J}^{-1}$ with all rows associated to zero stiffness joints removed. As such, $\mathbf{J}_e^{-1}$ maps an end-effector displacement twist on the elastic joint displacement vector $d\mathbf{q}_e$. Finally, matrix $\mathbf{K}_{q,e}$ is the stiffness matrix of the parallel manipulator expressed in the space spanned by the elastic joint coordinates, which includes the effect of actuated joints, compliant joints, as well as structural compliance. See the derivations in Hoevenaars et al. [20] for further detail.

A second approach to solving Eq. (7) for limited-DoF manipulators is by developing $\mathbf{M}$ and $\mathbf{K}$ in a full-rank subset of Cartesian coordinates, namely

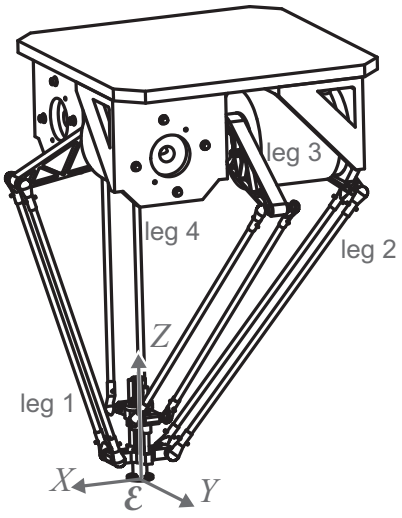

Figure 1: The Heli4 manipulator is modeled as a 4-RRΠRR robot. All twists, wrenches and matrices are expressed in the Cartesian end-effector reference frame $\mathcal{E}$.

only those DoFs that are actuated. This avoids the need to develop an expression for the structural stiffness of a limited-DoF parallel manipulator to produce a 6×6 matrix $\mathbf{K}$ that is full-rank. For example, a Delta robot can perform only linear motions, so Eq. (7) could also be developed using 3×3 matrices spanning the linear motions, instead of full 6×6 matrices. In this paper, this subset approach is used to perform an alternative natural frequency analysis, in which structural compliance is neglected and only actuator stiffness is considered. Then the traditional stiffness mapping from actuated joint space to Cartesian space can be used as introduced by Gosselin [11],

$$\mathbf{K}_R = \mathbf{J}_a^{-\top} \mathbf{K}_{q,a} \mathbf{J}_a^{-1} \tag{14}$$

where $\mathbf{K}_R$ represents the rigid-body stiffness matrix, $\mathbf{J}_a^{-1}$ is the inverse Jacobian matrix that maps an end-effector twist on the actuated joint coordinates, and $\mathbf{K}_{q,a}$ is the diagonal matrix containing the individual actuator stiffness values.

3. Example Analysis of Heli4 Manipulator

In this section the proposed natural frequency analysis method is applied to the Heli4 manipulator, which was developed by Krut et al. [35]. Figure 1

shows the structure of the Heli4, which has four identical legs. In this paper each leg is modeled as a RRΠRR serial chain, where R stands for a revolute joint and Π for a 1-DoF planar parallelogram joint. Because the analysis method that is developed in this paper is based on the full Jacobian analysis as presented by Huang et al. [33], the set of six independent unit twists and unit wrenches for each leg were developed first, and can be found in Appendix A. Note that each leg of the Heli4 manipulator has five degrees of freedom, so that for each leg one additional twist is derived that represents the constrained direction represented by a virtual joint.

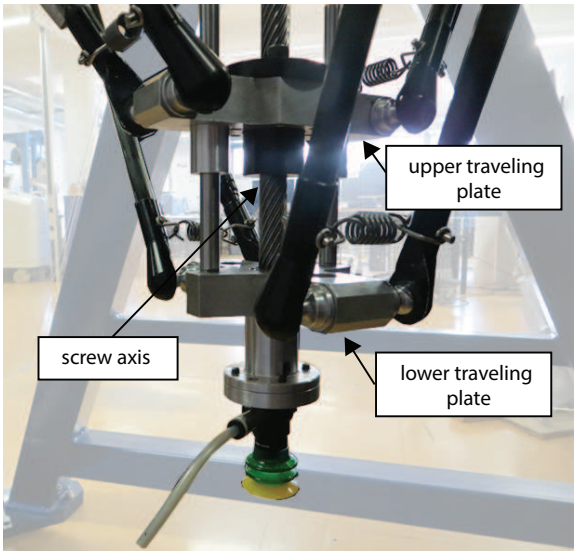

Figure 2: The end-effector assembly of the Heli4 manipulator facilitates the rotational motion of the end-effector by transforming a differential motion of the two traveling plates to rotational motion using a screw axis. In this paper it was found that friction prevented this rotational motion from being excited, so that in this paper the end-effector assembly is considered as a single body.

Although the Heli4 is a 4-DoF manipulator, whose end-effector can be controlled in three translations and a rotation around the Z-axis, in this paper it is analyzed as if it is a 3-DoF translational manipulator. This is because during the experimental verification it was found that the friction in the end-effector assembly, which enables the rotational motion of the end-effector, is of such magnitude that any induced motion is immediately damped out. As such, the end-effector assembly, of which a close-up is included in Fig. 2 is considered as a single body in the analysis performed in this paper.

In the remainder of this section, first the inertia analysis is performed using the method introduced in this paper. Next, two different stiffness analyses of the Heli4 robot are performed. One stiffness analysis is performed in which only actuator stiffness is considered. A second stiffness analysis is performed in which also link compliance and end-effector compliance are considered. Finally, for a specific reference pose two natural frequency analyses are performed by combining the inertia analysis with the rigid-body stiffness analysis and the flexible-body stiffness analysis respectively.

3.1. Inertia Analysis

To perform the inertia analysis as in Eq. (12), the full inverse Jacobian matrix for each leg, $\mathbf{J}_i^{-1}$ and the forward Jacobian matrices $\mathbf{J}_{i,j}$ are required. The full inverse Jacobian matrix for each individual legs is developed using the method described by Huang et al. [33] and the twists and wrenches as introduced in Appendix A,

$$\mathbf{J}_i^{-1} = \begin{bmatrix} \hat{\$}_{wa,i,1}^\top / (\hat{\$}_{wa,i,1}^\top \hat{\$}_{ta,i,1}) \\ \hat{\$}_{wa,i,2}^\top / (\hat{\$}_{wa,i,2}^\top \hat{\$}_{ta,i,2}) \\ \hat{\$}_{wa,i,3}^\top / (\hat{\$}_{wa,i,3}^\top \hat{\$}_{ta,i,3}) \\ \hat{\$}_{wa,i,4}^\top / (\hat{\$}_{wa,i,4}^\top \hat{\$}_{ta,i,4}) \\ \hat{\$}_{wa,i,5}^\top / (\hat{\$}_{wa,i,5}^\top \hat{\$}_{ta,i,5}) \\ \hat{\$}_{wc,i,1}^\top / (\hat{\$}_{wc,i,1}^\top \hat{\$}_{tc,i,1}) \end{bmatrix} \tag{15}$$

Because each leg is modeled as a 5-DoF chain, the forward Jacobian matrices can be developed as

$$\mathbf{J}_{i,1} = \begin{bmatrix} \hat{\$}_{ta,i,1} & \mathbf{0}_{6\times5} \end{bmatrix}, \tag{16}$$

$$\mathbf{J}_{i,2} = \begin{bmatrix} \hat{\$}_{ta,i,1} & \hat{\$}_{ta,i,2} & \mathbf{0}_{6\times4} \end{bmatrix}, \tag{17}$$

$$\mathbf{J}_{i,3} = \begin{bmatrix} \hat{\$}_{ta,i,1} & \hat{\$}_{ta,i,2} & \hat{\$}_{ta,i,3} & \mathbf{0}_{6\times3} \end{bmatrix}, \tag{18}$$

$$\mathbf{J}_{i,4} = \begin{bmatrix} \hat{\$}_{ta,i,1} & \hat{\$}_{ta,i,2} & \hat{\$}_{ta,i,3} & \hat{\$}_{ta,i,4} & \mathbf{0}_{6\times2} \end{bmatrix}, \tag{19}$$

$$\mathbf{J}_{i,5} = \begin{bmatrix} \hat{\$}_{ta,i,1} & \hat{\$}_{ta,i,2} & \hat{\$}_{ta,i,3} & \hat{\$}_{ta,i,4} & \hat{\$}_{ta,i,5} & \mathbf{0}_{6\times1} \end{bmatrix}. \tag{20}$$

Also, the matrices $\mathbf{M}_{i,j}$ need to be developed. These matrices need to be expressed in the same Cartesian reference frame as in which all unit twists

and unit wrenches are expressed. In this paper, all twists and wrenches are expressed in the Cartesian end-effector reference frame $\mathcal{E}$ shown in Fig. 1. However, usually inertia matrices are more easily obtained in a local reference frame. Therefore, in this paper adjoint matrices are used to transform such locally expressed matrices into end-effector Cartesian space. For the example analysis of the Heli4 in this paper, some of these matrices will be expressed analytically while others will be extracted from the CAD model.

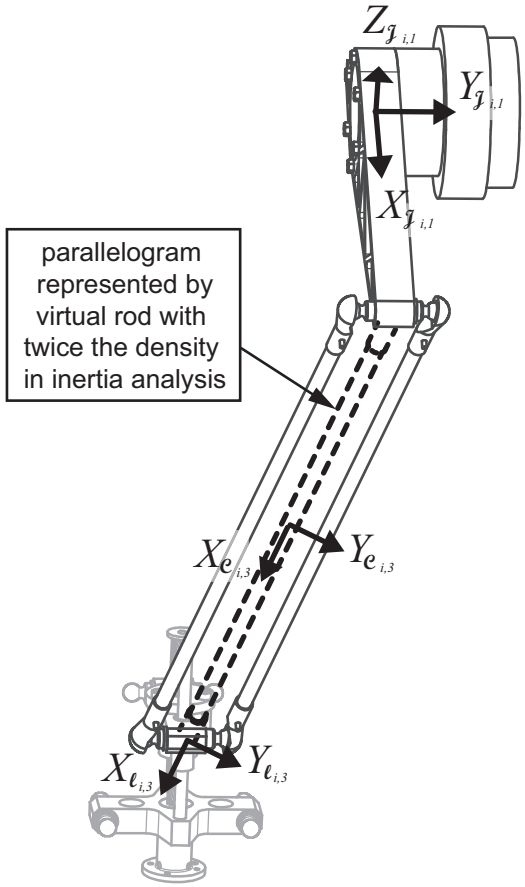

Figure 3: The inertia of the first link and the actuator are expressed in reference frame $\mathcal{J}_{i,1}$. To represent the inertia of the parallelogram it is modeled as a single rod, positioned midway between the two parallel rods, with double the mass density.

The inertia matrix of the first body, which is connected to the actuated

joint, can be expressed as

$$\mathbf{M}_{i,1}^{\mathcal{J}_{i,1}} = \mathbf{M}_{i,1,a}^{\mathcal{J}_{i,1}} + \mathbf{M}_{i,1,l}^{\mathcal{J}_{i,1}} \tag{21}$$

where $\mathbf{M}_{i,1,a}^{\mathcal{J}_{i,1}}$ is the inertia matrix of the actuator rotor, and $\mathbf{M}_{i,1,l}^{\mathcal{J}_{i,1}}$ is the inertia of the link which is rigidly connected this rotor, both expressed in the local Cartesian reference frame $\mathcal{J}_{i,1}$ as shown in Fig. 3. Because the only motion that the rotor can make is rotation around its local Y-axis, the angular momentum around its axis is the only relevant inertia. For the Heli4, it is therefore sufficient to express $\mathbf{M}_{i,1,a}^{\mathcal{J}_{i,1}}$ as

$$\mathbf{M}_{i,1,a}^{\mathcal{J}_{i,1}} = \mathrm{diag}\left([0 \quad \text{4.1e-3} \quad 0 \quad 0 \quad 0 \quad 0]\right). \tag{22}$$

The inertia of the link that is rigidly connected to the axis is obtained from the CAD model as

$$\mathbf{M}_{i,1,l}^{\mathcal{J}_{i,1}} = \begin{bmatrix} 0.0003 & 0 & 0 & 0 & 0 & 0 \\ 0 & 0.0044 & 0 & 0 & 0 & -0.0293 \\ 0 & 0 & 0.0042 & 0 & 0.0293 & 0 \\ 0 & 0 & 0 & 0.479 & 0 & 0 \\ 0 & 0 & 0.0293 & 0 & 0.479 & 0 \\ 0 & -0.0293 & 0 & 0 & 0 & 0.479 \end{bmatrix} \tag{23}$$

The inertia matrix expressed by Eq. (21) can be expressed in the end-effector Cartesian reference frame using the transformation

$$\mathbf{M}_{i,1} = \mathbf{Ad}_{\mathbf{H}_{\mathcal{E}}^{\mathcal{J}_{i,1}}}^{\top} \mathbf{M}_{i,1}^{\mathcal{J}_{i,1}} \mathbf{Ad}_{\mathbf{H}_{\mathcal{E}}^{\mathcal{J}_{i,1}}} \tag{24}$$

where $\mathbf{Ad}_{\mathbf{H}_{\mathcal{E}}^{\mathcal{J}_{i,1}}}$ is the adjoint matrix associated to the homogeneous transformation matrix $\mathbf{H}_{\mathcal{E}}^{\mathcal{J}_{i,1}}$, which transforms a vector expressed in the end-effector reference frame into the Cartesian reference frame in which $\mathbf{M}_{i,1}^{\mathcal{J}_{i,1}}$ is expressed. For more details on adjoint matrices and homogeneous matrices, see e.g. Murray et al. [36].

In this paper, some simplifications are made in the expression of the inertia of the remaining bodies of each leg. Firstly, because the second R-joint and the top part of the Π-joint are collocated, there is no physical body located between these joints. Therefore, for each leg the contribution of the body with index 2 is zero. The same holds for the bodies with index 4 and 5. Then,

$$\mathbf{M}_{i,2} = \mathbf{M}_{i,4} = \mathbf{M}_{i,5} = \mathbf{0}_{6\times 6} \tag{25}$$

Table 1: Values of various parameters of the Heli4 manipulator

description	symbol	value	unit
length of lower link	l_1	0.20	m
length of parallelogram	l_2	0.53	m
distance to cog of 1st rod	$l_{1,cog}$	0.0612	m
inner radius of rods	r_i	3.5	mm
outer radius of rods	r_o	5.0	mm
density of rods	ρ	2000	kg/(m^3)
parallelogram width	w_Π	55	mm

Secondly, it is assumed that the inertia of the parallelogram that is part of the Π-joint can be modeled as the inertia of a single tube with double the density of the original bars in the parallelogram positioned as in Fig. 3. The inertia matrix can then be expressed in its fictitious center of gravity as,

$$\mathbf{M}_{i,3}^{\mathcal{C}_{i,3}} = \begin{bmatrix} I_x & 0 & 0 & 0 & 0 & 0 \\ 0 & I_y & 0 & 0 & 0 & 0 \\ 0 & 0 & I_z & 0 & 0 & 0 \\ 0 & 0 & 0 & m & 0 & 0 \\ 0 & 0 & 0 & 0 & m & 0 \\ 0 & 0 & 0 & 0 & 0 & m \end{bmatrix} \tag{26}$$

where the reference frame $\mathcal{C}_{i,3}$ is also illustrated in Fig. 3 and

$$I_x = \frac{m}{2}\left(r_i^2 + r_o^2\right) \tag{27}$$

$$I_y = I_z = \frac{m}{12}\left(3\left(r_i^2 + r_o^2\right) + (l_2)^2\right) \tag{28}$$

$$m = 2l_2\rho\pi\left(r_o^2 - r_i^2\right). \tag{29}$$

The factor two in Eq. (29) accounts for the fact that a single fictitious link is used to represent the two links of the parallelogram. For the Heli4, the values of the various parameters in Eqs. (27)-(29) can be found in Table 1.

Since the inertia matrix in Eq. (26) is expressed in the Cartesian reference frame located at the center of gravity of the fictitious link that replaces the

parallelogram, the matrix in Eq. (26) must be transformed to end-effector Cartesian space,

$$\mathbf{M}_{i,3} = \mathbf{Ad}^{\top}_{\mathbf{H}_{\mathcal{E}}^{\mathcal{C}_{i,3}}} \mathbf{M}_{i,3}^{\mathcal{C}_{i,3}} \mathbf{Ad}_{\mathbf{H}_{\mathcal{E}}^{\mathcal{C}_{i,3}}} \tag{30}$$

where $\mathbf{Ad}_{\mathbf{H}_{\mathcal{E}}^{\mathcal{C}_{i,3}}}$ is the adjoint matrix associated to the homogeneous transformation matrix $\mathbf{H}_{\mathcal{E}}^{\mathcal{C}_{i,3}}$, which transforms a vector expressed in end-effector Cartesian space into the equivalent vector in the Cartesian space at the center of gravity of the fictitious parallelogram link.

The last matrix required to evaluate Eq. (12) for the Heli4 manipulator is the end-effector inertia matrix. Because the manipulator is modeled as if the rotational motion is fixed, the complete end-effector assembly is considered as a single end-effector. The inertia matrix of the complete end-effector assembly is obtained from the CAD model as

$$\mathbf{M}_e = \begin{bmatrix} 0.009 & 0 & 0 & 0 & 0 & 0 \\ 0 & 0.009 & 0 & 0 & 0 & 0 \\ 0 & 0 & 0.001 & 0 & 0 & 0 \\ 0 & 0 & 0 & 0.592 & 0 & 0 \\ 0 & 0 & 0 & 0 & 0.592 & 0 \\ 0 & 0 & 0 & 0 & 0 & 0.592 \end{bmatrix} \tag{31}$$

which is directly expressed in Cartesian end-effector space, i.e. the top-left three values are the moments of inertia around the X-, Y, and Z-axis respectively (kg·m^2), and the three lower-right values are the mass value (kg). Off-diagonal terms were of such small magnitude that they amounted to zero when rounded to three decimal places.

If the expressions that were introduced in Eqs. (24), (25), and (30) are inserted in Eq. (12), and considering that Heli4 has four legs, its inertia can be expressed as

$$\begin{aligned} \mathbf{M} = \sum_{i=1}^{4} \Big(& \mathbf{J}_i^{-\top} \mathbf{J}_{i,1}^{\top} \mathbf{Ad}^{\top}_{\mathbf{H}_e^{\mathcal{J}_{i,1}}} \mathbf{M}_{i,1}^{\mathcal{J}_{i,1}} \mathbf{Ad}_{\mathbf{H}_e^{\mathcal{J}_{i,1}}} \mathbf{J}_{i,1} \mathbf{J}_i^{-1} \\ & + \mathbf{J}_i^{-\top} \mathbf{J}_{i,3}^{\top} \mathbf{Ad}^{\top}_{\mathbf{H}_e^{\mathcal{C}_{i,3}}} \mathbf{M}_{i,3}^{\mathcal{C}_{i,3}} \mathbf{Ad}_{\mathbf{H}_e^{\mathcal{C}_{i,3}}} \mathbf{J}_{i,3} \mathbf{J}_i^{-1} \Big) + \mathbf{M}_e \end{aligned} \tag{32}$$

where the necessary Jacobian matrices where expressed in Eqs. (15)-(20).

3.2. Stiffness Analysis

As described at the end of Section 2, the natural frequency analysis is performed by combining the presented rigid-body inertia analysis with two different stiffness models:

1. *Rigid-body stiffness model* where only actuator compliance is considered, making use of Eq. (14)
2. *Flexible-body stiffness model* where the compliance of the parallelograms and the end-effector assembly is considered, making use of Eq. (13)

3.2.1. Rigid-body stiffness model

To perform a rigid-body stiffness analysis, Eq. (14) is used, where

$$\mathbf{J}_a^{-1} = \begin{bmatrix} \hat{\$}_{wa,1,1}^\top / (\hat{\$}_{wa,1,1}^\top \hat{\$}_{ta,1,1}) \\ \hat{\$}_{wa,2,1}^\top / (\hat{\$}_{wa,2,1}^\top \hat{\$}_{ta,2,1}) \\ \hat{\$}_{wa,3,1}^\top / (\hat{\$}_{wa,3,1}^\top \hat{\$}_{ta,3,1}) \\ \hat{\$}_{wa,4,1}^\top / (\hat{\$}_{wa,4,1}^\top \hat{\$}_{ta,4,1}) \end{bmatrix} \tag{33}$$

is the Jacobian that maps an end-effector twist on the four actuated base joints, constructed from the twists and wrenches introduced in Appendix A, and

$$\mathbf{K}_{q,a} = \mathrm{diag}\left(0.82 \begin{bmatrix} k_a & k_a & k_a & k_a \end{bmatrix}\right) \tag{34}$$

is the stiffness matrix in joint space which consists of the four controlled actuator stiffness values. It should be noted that there is a factor 0.82 difference between the commanded actuator stiffness and the controlled actuator stiffness, which is explained in Appendix B.

Since the Heli4 manipulator is considered as a 3-DoF translational manipulator, the resulting matrix $\mathbf{K}_R$ is only defined for the three translational directions.

3.2.2. Flexible-body stiffness model

To perform the flexible-body stiffness analysis as in Eq. (13) several vectors and matrices are required. The full inverse Jacobian matrix $\mathbf{J}^{-1}$ can be assembled as

$$\mathbf{J}^{-1} = \begin{bmatrix} \mathbf{J}_1^{-1} \\ \mathbf{J}_2^{-1} \\ \mathbf{J}_3^{-1} \\ \mathbf{J}_4^{-1} \end{bmatrix} \tag{35}$$

where each matrix $\mathbf{J}_i^{-1}$ is the full inverse Jacobian matrices for the ith leg as introduced in Eq. (15).

The inverse Jacobian of elasticity, $\mathbf{J}_e^{-1}$, is obtained by removing those rows from $\mathbf{J}_i^{-1}$ that are associated with zero stiffness joints. In the Heli4 the first R-joint of each leg counted from the base is actuated, while the other RIIRR joints are all zero stiffness joints. The virtual joint that represents the constrained motion of each leg has a none-zero stiffness which is a function of the structural compliance. As such,

$$\mathbf{J}_e^{-1} = \begin{bmatrix} \mathbf{J}_{e,1}^{-1} \\ \mathbf{J}_{e,2}^{-1} \\ \mathbf{J}_{e,3}^{-1} \\ \mathbf{J}_{e,4}^{-1} \end{bmatrix} \tag{36}$$

where for each leg i,

$$\mathbf{J}_{e,i}^{-1} = \begin{bmatrix} \hat{\$}_{wa,i,1}^{\top} / (\hat{\$}_{wa,i,1}^{\top} \hat{\$}_{ta,i,1}) \\ \hat{\$}_{wc,i,1}^{\top} / (\hat{\$}_{wc,i,1}^{\top} \hat{\$}_{tc,i,1}) \end{bmatrix} \tag{37}$$

In this paper the manipulator is assumed to operate around an unloaded reference pose, which means that the actuator forces required to overcome gravitational forces are neglected. Then,

$$\boldsymbol{\tau}_e = \mathbf{0} \tag{38}$$

and therefore

$$\left(-\frac{\partial \mathbf{J}_e^{-\top}}{\partial \mathbf{q}} \boldsymbol{\tau}_e \right) \mathbf{J}^{-1} = \mathbf{0} \tag{39}$$

The final unknown in Eq. (13) is $\mathbf{K}_{q,e}$, which represents the stiffness of the Heli4 manipulator in its joint space. As described in Ref. [20], this matrix is constructed as

$$\mathbf{K}_{q,e} = \begin{bmatrix} \mathbf{K}_{q,e,1} & \mathbf{0} & \mathbf{0} & \mathbf{0} \\ \mathbf{0} & \mathbf{K}_{q,e,2} & \mathbf{0} & \mathbf{0} \\ \mathbf{0} & \mathbf{0} & \mathbf{K}_{q,e,3} & \mathbf{0} \\ \mathbf{0} & \mathbf{0} & \mathbf{0} & \mathbf{K}_{q,e,4} \end{bmatrix} \tag{40}$$

where each matrix $\mathbf{K}_{q,e,i}$ can be obtained by (numerically) inverting the summation

$$\mathbf{K}_{q,e,i}^{-1} = \mathbf{K}_{q,e,k,i}^{-1} + \mathbf{K}_{q,e,s,i}^{-1} \tag{41}$$

in which $\mathbf{K}^{-1}_{q,e,k,i}$ is the compliance localized in the kinematic joints and $\mathbf{K}^{-1}_{q,e,s,i}$ is a representation in the elastic joint space of the structural compliance of all links that make up the ith leg. Both matrices are 2×2 matrices, because each leg has two joint coordinates in which the manipulator has a finite stiffness, namely the actuated joint and the virtual joint that represent the constraint. For the virtual joints there is no locally defined joint compliance, while the actuated joints of the Heli4 manipulator were commanded by a proportional controller with a stiffness k_a, so that

$$\mathbf{K}^{-1}_{q,e,k,i} = \begin{bmatrix} (0.82k_a)^{-1} & 0 \\ 0 & 0 \end{bmatrix} \tag{42}$$

where the factor 0.82 is included to account for the losses in the torque generation as mentioned after Eq. (34).

The matrix $\mathbf{K}^{-1}_{q,e,s,i}$ represents the structural compliance of the individual links in the ith leg, projected onto its elastic joint space,

$$\mathbf{K}^{-1}_{q,e,s,i} = \mathbf{J}^{-1}_{e,i}\mathbf{K}^{-1}_{s,i}\mathbf{J}^{-\top}_{e,i} \tag{43}$$

where $\mathbf{J}^{-1}_{e,i}$ was introduced in Eq. (37) and $\mathbf{K}^{-1}_{s,i}$ is the structural compliance of the links in the ith leg expressed in the Cartesian end-effector reference frame. The latter matrix will be developed next.

For the Heli4 robot the structural compliance of all links is considered negligible, except for the rods that form the parallelogram. An expression for the structural compliance of the two rods that form each parallelogram is derived analytically in Appendix C. To express this local compliance in the Cartesian end-effector reference frame, use is made of the transformation

$$\mathbf{K}^{-1}_{\Pi,i} = \mathbf{Ad}_{\mathbf{H}^{\mathcal{E}}_{\ell_{i,3}}}\mathbf{K}^{-1}_{\Pi,\ell_{i,3}}\mathbf{Ad}^{\top}_{\mathbf{H}^{\mathcal{E}}_{\ell_{i,3}}} \tag{44}$$

where $\mathbf{Ad}_{\mathbf{H}^{\mathcal{E}}_{\ell_{i,3}}}$ is the adjoint matrix that maps a twist which is expressed in the reference frame $\ell_{i,3}$ (see Fig. 3) onto the Cartesian end-effector reference frame. This adjoint matrix is thus a function of the pose of the manipulator. It should be noted that the matrix $\mathbf{K}^{-1}_{\Pi,i}$ represents the compliance of the links in the parallelogram as if they were cantilever beams connected to the leading link. The mobility in the parallelogram is covered by the Jacobian mappings in Eq. (43), which removes those direction from the stiffness analysis and thereby attributes zero stiffness to those joints.

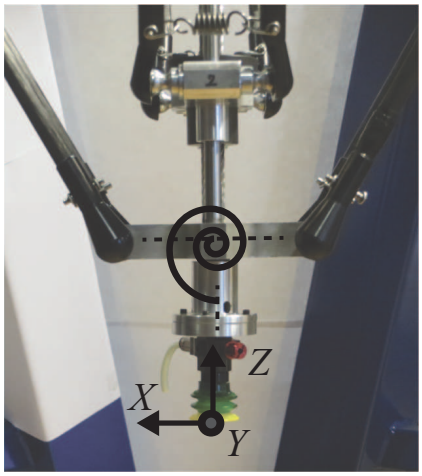

Figure 4: It was found that structural compliance in the end-effector assembly of the Heli4 manipulator is significant and that this can be represented by a rotational stiffness of 500 Nm/rad and a linear stiffness of $1.3e5$ N/m around the Y-axis located at the center of the lower traveling plate (center of schematic spring).

During the tests it was realized that the end-effector assembly forms a significant, additional source of structural compliance in the Heli4 robot. Using a simple test, which is described in Appendix D, the stiffness of the assembly was identified as 500 Nm/rad when modeled as a rotational compliance along the Y-axis and located in the center of the lower traveling plate, and a linear stiffness of $1.3e5$ N/m along the same Y-axis, see Fig. 4. However, existing methods for the stiffness analysis of parallel manipulators do not allow for integration of end-effector stiffness. Therefore, based on the rule of stiffness addition in parallel, the identified structural stiffness of the end-effector is divided over the four legs. For the case that the end-effector is located on the central axis of the robot, so that legs 1 and 2 are aligned with the X-axis and legs 3 and 4 are aligned with the Y-axis, this division can be done as

following:

$$\mathbf{K}_{E,ltp,1}^{-1} = \text{diag}\left(\begin{bmatrix} 0 & \frac{1}{0.5k_{E,rot}} & 0 & 0 & 0 & 0 \end{bmatrix}\right) \tag{45}$$

$$\mathbf{K}_{E,ltp,2}^{-1} = \text{diag}\left(\begin{bmatrix} 0 & \frac{1}{0.5k_{E,rot}} & 0 & 0 & 0 & 0 \end{bmatrix}\right) \tag{46}$$

$$\mathbf{K}_{E,ltp,3}^{-1} = \text{diag}\left(\begin{bmatrix} 0 & 0 & 0 & 0 & \frac{1}{0.5k_{E,lin}} & 0 \end{bmatrix}\right) \tag{47}$$

$$\mathbf{K}_{E,ltp,4}^{-1} = \text{diag}\left(\begin{bmatrix} 0 & 0 & 0 & 0 & \frac{1}{0.5k_{E,lin}} & 0 \end{bmatrix}\right). \tag{48}$$

where $\mathbf{K}_{E,ltp,i}^{-1}$ is the compliance matrix of the lower traveling plate with respect to the upper traveling plate, expressed in a reference frame at the center of the lower traveling plate. These matrices can be expressed in end-effector Cartesian space using

$$\mathbf{K}_{E,i}^{-1} = \mathbf{Ad}_{\mathbf{H}_{ltp}^{\mathcal{E}}} \mathbf{K}_{E,ltp,i}^{-1} \mathbf{Ad}_{\mathbf{H}_{ltp}^{\mathcal{E}}}^{\top} \tag{49}$$

where $\mathbf{Ad}_{\mathbf{H}_{ltp}^{\mathcal{E}}}$ is the adjoint matrix corresponding to a linear transformation along the Z-axis of 78 mm, and which maps the respective end-effector compliance matrix onto the Cartesian end-effector reference frame that is used throughout this paper. The structural compliance matrix for each leg is the sum of the contributions by the links that make up the parallelogram and by the end-effector assembly,

$$\mathbf{K}_{s,i}^{-1} = \mathbf{K}_{\Pi,i}^{-1} + \mathbf{K}_{E,i}^{-1}. \tag{50}$$

Next, Eq. (50) can be inserted in Eq. (43) and subsequently combined with Eq. (42) to express the total compliance of each individual leg in its elastic joint space, $\mathbf{K}_{q,e,i}^{-1}$. After (numerical) inversion, the resulting stiffness matrices of individual legs can be inserted in Eq. (40). With that, all elements of Eq. (13) have been expressed for the Heli4 robot.

3.3. Natural Frequency Analysis

The stiffness matrices $\mathbf{K}_R$ or $\mathbf{K}_F$ developed in Section 3.2 can be combined with the inertia analysis as expressed in Eq. (32) to perform the natural frequency analysis as in Eq. (7). For a given pose of the end-effector, the inertia matrix and the structural compliance of the various links in the Heli4 are fixed, but the actuator stiffness can be controlled.

As an example, the natural frequency analysis is performed at the position

$$\mathbf{x}_{ref} = [0 \quad 0 \quad -0.625]^\top \tag{51}$$

with respect to the Cartesian reference frame with its origin at the center of the four actuated joints and its axes parallel to the end-effector reference frame. The actuator stiffness was set at $k_a = 2000$ Nm/rad. At this pose, the end-effector inertia matrix is evaluated as

$$\mathbf{M}|_{\mathbf{x}_{ref}} = \begin{bmatrix} 0.012 & 0 & 0 & 0 & -0.031 & 0 \\ 0 & 0.013 & 0 & 0.027 & 0 & 0 \\ 0 & 0 & 0.001 & 0 & 0 & 0 \\ 0 & 0.027 & 0 & 0.953 & 0 & 0 \\ -0.031 & 0 & 0 & 0 & 0.983 & 0 \\ 0 & 0 & 0 & 0 & 0 & 1.556 \end{bmatrix}. \tag{52}$$

For the end-effector stiffness matrix two models have been developed, which are subsequently evaluated below.

3.3.1. Rigid-body model

When the rigid-body Cartesian end-effector stiffness matrix resulting from Eq. (14) is analyzed at the example pose and with $k_a = 2000$ Nm/rad, the result is

$$\mathbf{K}_R|_{\mathbf{x}_{ref}} = \begin{bmatrix} 103 & 0 & 0 & 0 & -1668 & 0 \\ 0 & 0 & 0 & -96 & 0 & 0 \\ 0 & 0 & 0 & 0 & 0 & 0 \\ 0 & -96 & 0 & 20785 & 0 & 0 \\ -1668 & 0 & 0 & 0 & 26875 & 0 \\ 0 & 0 & 0 & 0 & 0 & 128857 \end{bmatrix}. \tag{53}$$

As can be observed, the rigid-body stiffness matrix in Eq. (53) is not full-rank, which is expected for a limited-DoF parallel manipulator. This is not a problem, because the motions of interest are the linear motions. Therefore subsets of the matrices in Eqs. (53) and (52) can be used for a natural frequency analysis of the rigid-body model. More specifically, because the Heli4 was considered as a 3-DoF linear robot, the lower-right 3×3 matrices are used.

If lower-right 3×3 subsets of the matrices in Eqs. (52) and (53) are inserted in Eq. (7) to calculate the three eigenfrequencies, the results are

$$\omega_1 = 23.5 \text{ Hz} \tag{54}$$

$$\omega_2 = 26.3 \text{ Hz} \tag{55}$$

$$\omega_3 = 45.8 \text{ Hz} \tag{56}$$

whose corresponding eigentwists can be obtained by inserting them in Eq. (6), resulting in

$$\$_{v,1-3} = \begin{bmatrix} 1.000 & 0 & 0 \\ 0 & 1.000 & 0 \\ 0 & 0 & 1.000 \end{bmatrix} \tag{57}$$

which is the matrix containing from left to right the three eigentwists in the analyzed subset of linear motions when the rigid-body stiffness model is considered.

3.3.2. Flexible-body model

When the flexible-body Cartesian end-effector stiffness matrix resulting from Eq. (13) is analyzed at the example pose and with $k_a = 2000$ Nm/rad, the result is

$$\mathbf{K}_F|_{\mathbf{x}_{ref}} = \begin{bmatrix} 29501 & 0 & 0 & 0 & -1380 & 0 \\ 0 & 28114 & 0 & -74 & 0 & 0 \\ 0 & 0 & 21159 & 0 & 0 & 0 \\ 0 & -74 & 0 & 16170 & 0 & 0 \\ -1380 & 0 & 0 & 0 & 22233 & 0 \\ 0 & 0 & 0 & 0 & 0 & 103566 \end{bmatrix} \tag{58}$$

The flexible-body stiffness matrix in Eq. (58) is full-rank, because stiffness in the constrained directions is included.

If Eqs. (52) and (58) are inserted in Eq. (7) to calculate the six eigenfrequencies, the results are

$$\omega_1 = 20.7 \text{ Hz} \tag{59}$$

$$\omega_2 = 23.9 \text{ Hz} \tag{60}$$

$$\omega_3 = 41.1 \text{ Hz} \tag{61}$$

$$\omega_4 = 246.0 \text{ Hz} \tag{62}$$

$$\omega_5 = 262.6 \text{ Hz} \tag{63}$$

$$\omega_6 = 635.8 \text{ Hz} \tag{64}$$

Table 2: Imposed actuator stiffness values to evaluate natural frequencies after step input

	Nm/rad
$k_{a,1}$	125
$k_{a,2}$	250
$k_{a,3}$	500
$k_{a,4}$	1000
$k_{a,5}$	1500
$k_{a,6}$	2000
$k_{a,7}$	3000
$k_{a,8}$	4000

whose corresponding eigentwists can be obtained by inserting them in Eq. (6), resulting in

$$\$_{v,1-6} = \begin{bmatrix} 0 & 0.023 & 0 & 0 & 1.000 & 0 \\ 0.019 & 0 & 0 & 1.000 & 0 & 0 \\ 0 & 0 & 0 & 0 & 0 & 1.000 \\ 1.000 & 0 & 0 & -0.029 & 0 & 0 \\ 0 & 1.000 & 0 & 0 & 0.031 & 0 \\ 0 & 0 & 1.000 & 0 & 0 & 0 \end{bmatrix} \tag{65}$$

which is the matrix containing, from left to right, the six eigentwists for the case that the flexible-body stiffness model is used.

4. Verification Method of Natural Frequencies

To verify the natural frequency analysis, the Heli4 robot was excited in its two lowest natural frequencies, for the actuator stiffness values introduced in Table 2. As can be seen from both Eqs. (57) and (65), the eigentwists associated to the two lowest natural frequencies can be excited by imposing a step function in the X-direction and Y-direction respectively. Step functions of 100 mm are imposed along either direction. These step functions will be imposed by setting the corresponding actuator reference positions, as are calculated using the inverse kinematics, which are described by Krut et al. [35]. A damping of 3 Nm·s/rad was added to the actuator controllers to prevent

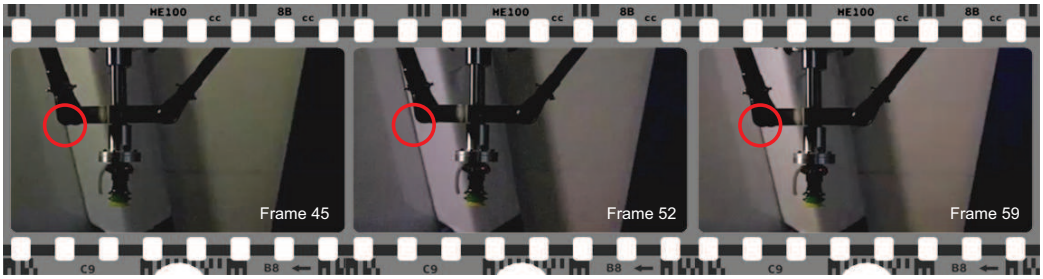

Figure 5: A series of frames from one of the high-speed video for the step response in X-direction with a actuator stiffness of 2000 Nm/rad. The frames capture one oscillation going from left to right and back, which can for example be observed in the red circles by the relative motion of the end-effector with respect to the background.

damage to the system. This damping is sufficiently low not to affect the natural frequencies. The actuator stiffness values were implemented by means of a proportional feedback controller on the joint angle of each of the four actuated joints.

To measure the natural frequencies, a high-speed camera was used, because this allowed an independent measurement of the end-effector oscillations. A Canon EX-F1 camera was used, capturing video at 300 frames per second. To measure the frequency of the induced oscillations, a simple calculation was made based on the number of frames taken for a counted number of oscillations. Figure 5 shows a series of images from an imposed step function in the X-direction on the reference position for an actuator stiffness of 2000 Nm/rad.

5. Results

The results of the natural frequency analysis and the verification activities are summarized in Fig. 6. Based on the analysis introduced in this paper the first and second natural frequencies are predicted for actuator stiffness values up to 4000 Nm/rad. This prediction is done both using a rigid-body stiffness model and a flexible-body stiffness model. Overlaid are the measured natural frequencies for the implemented actuator stiffness values as introduced in Table 2. All natural frequencies have been converted from rad/s to Hz for ease of interpretation.

The figure shows that the predicted values for ω_1 and ω_2 are more accurate if the flexible-body stiffness model is used. Compared to the predictions

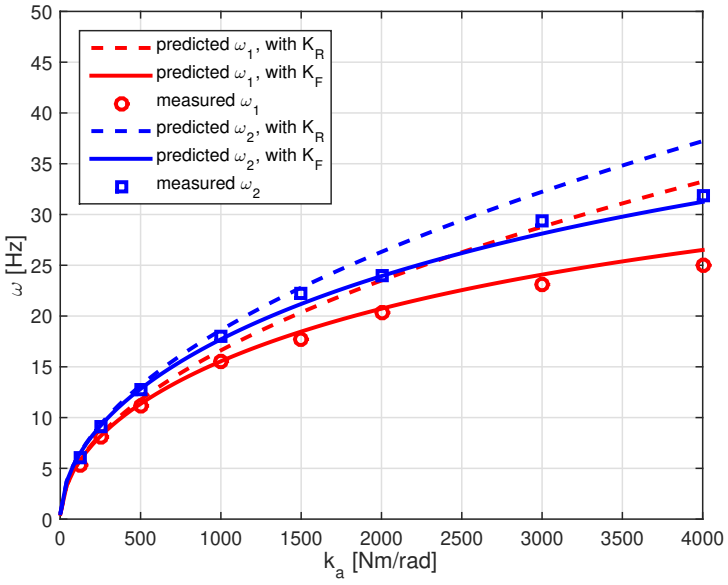

Figure 6: The predicted values for the two lowest natural frequencies, using either the rigid-body stiffness model or the flexible-body stiffness model, as well as the measured natural frequencies as a function of actuator stiffness values.

based on a rigid-body stiffness model, the values decrease and become more accurate. For example, the error in the predicted value for ω_1 at $k_a = 4000$ Nm/rad reduces from 33% to 6%. The difference between the predicted and the measured value for ω_2 at an actuator stiffness of 4000 Nm/rad reduces from 17% to 2%.

The high-speed videos that were used to determine the values for the measured ω_1 and ω_2 can be downloaded as supplementary material to this paper. During the experimental verification also data regarding the state of the robot was recorded, which was used to determine the loss factor of 0.82 discussed in Appendix B, and to confirm that no significant end-effector rotation was induced. These data are also available as supplementary material to this paper. Appendix E presents an analysis of the significance of the two considered sources of structural compliance, showing that the end-effector assembly is the dominant source of compliance for the example analysis presented in this paper.

6. Discussion

As can be seen from Fig. 6, for actuator stiffness values up to roughly 1000 Nm/rad all predicted values show close agreement with the measured natural frequencies. This implies that the developed inertia model as well as both the stiffness models are accurate for that range of actuator stiffness values. As such, for this range of actuator stiffness values, a flexible-body stiffness analysis has no added value over a rigid-body stiffness analysis. In short, up to actuator stiffness values of 1000 Nm/rad the Heli4 manipulator dynamics are accurately described by rigid body motion and controlled actuator stiffness.

However, the story is different for higher actuator stiffness values. The graphs in Fig. 6 illustrate that the predicted values for ω_1 and ω_2 closely agree with the measurements over the full range of actuator stiffness values only if the flexible-body model is used. It should be noted that the inertia model is kept the same for both analyses, namely based on rigid body motion. This indicates, at least for the example case, that the kinetic energy in the link deformations can be neglected as expected. Likewise, a rigid-body inertia model may be a good starting point for the analysis of other manipulators.

The idea to separate the inertia model and stiffness model was introduced to keep the dynamic model as simple as possible. In the presented example this was achieved by combining a rigid-body inertia model with a

stiffness model in which actuator stiffness as well as mechanical compliance was considered. Two sources of mechanical compliance were included in the analysis, namely the rods in the parallelograms, and the end-effector assembly. The compliance of the parallelogram links was included on the basis of linear beam theory, while the compliance of the end-effector assembly was included on the basis of experimental values. For the example analysis it was found that the end-effector assembly is the dominant source of structural compliance, but for other robotic manipulators there may be other sources of compliance that dominate the dynamic behavior, such as compliance in joint assemblies and/or transmission assemblies [37, 38]. As such, it will be up to the engineer to determine the required level of detail in the stiffness model.

Next, empowered with a verified model that describes the lowest natural frequencies of the Heli4 robot, an engineer can suggest improvements to the robot, and model the expected impact of those improvements. For example, the linear guides in the end-effector assembly could be replaced for alternatives that better constrain the motion described in Appendix D. After the improvement, the stiffness measurements of Appendix D can be repeated, and the new stiffness values can be inserted in the model to assess the expected impact on the overall robot performance.

It should also be noted that the current paper has analyzed the impact of structural compliance only in a single pose. This was done to deal with the distribution of the end-effector assembly compliance over the four legs. No existing Jacobian-based stiffness analysis has been found in the literature that can cope with end-effector compliance, while it was found to be a dominant factor for the Heli4 manipulator. As such, the absence of a general expression for the impact of end-effector stiffness on the overall stiffness is limiting the extension of the presented method to more complex poses of the Heli4 robot. How to include end-effector compliance in a Jacobian-based stiffness analysis of parallel manipulators is therefore an interesting open research question.

Because the presented natural frequency analysis is developed in the Cartesian end-effector reference frame, it relies on 6×6 stiffness and inertia matrices. As a result, six natural frequencies and corresponding eigentwists are predicted using the analysis. This means that for the case of limited-DoF parallel manipulators it is necessary to either consider structural compliance in the links, or to perform the natural frequency analysis on a subset of the Cartesian end-effector space that is full-rank.

If structural compliance is considered for a limited-DoF parallel manip-

ulators with N DoFs, and a full-rank Cartesian end-effector stiffness matrix and inertia matrix are obtained, $6-N$ natural frequencies will be associated to kinematically constrained directions. For example, the Heli4 robot was modeled in this paper as a 3-DoF manipulator. This means that only three natural frequencies correspond to kinematically allowed motions of the robot. The other three eigentwist in Eq. (65) include motions in the constrained directions of one or more legs of the manipulator. In these constrained directions the contribution by elastically deforming bodies to the inertia may no longer be negligible. As such, it may be expected that the predicted natural frequencies for the constrained directions will not be accurate, although this was not investigated in this paper.

The fact that natural frequencies in constrained directions might not be accurately predicted does not reduce the relevance of the proposed method. After all, the dynamic performance of parallel manipulators is limited by the set of lowest natural frequencies, which will generally occur in the kinematically allowed DoFs. Stiffness of a parallel manipulator is generally higher in the constrained directions than in the kinematic DoFs.

The main advantage of the developed analysis method over comparable methods is the focus on minimal model complexity by decoupling the level of detail in the stiffness model from the level of detail in the inertia model. Furthermore, the proposed method is presented in closed-form and does not rely on e.g. iterative schemes. The method is based on the transformation of locally expressed compliance and inertia matrices, which are typically directly available from linear beam theory or CAD software. Those transformations are performed using adjoint matrices and Jacobian matrices, which are a function of design variables and state variables. As such, the presented method provides a closed-form expression to calculate the natural frequencies. Minimal complexity and a closed-form expression could make the presented method an interesting candidate for design analysis, optimization, or use in model-based controllers as those presented by Callegari et al. [15] and Du and Lou [39].

7. Conclusions

This paper has developed a method to analyze the set of lowest natural frequencies of a parallel manipulator. The proposed method combines a flexible-body Cartesian stiffness model with a novel expression for the rigid-body Cartesian inertia model. While flexible-body stiffness models have

been extensively discussed in the literature, the combination with a rigid-body inertia model in Cartesian end-effector space is new. The inertia model is based on a Jacobian mapping of the end-effector twist on each individual body. This approach enables a structured addition of the contribution of each individual body to the overall inertia and, once a manipulator is defined, the resulting expression is only a function of the end-effector pose.

Because a rigid-body inertia model can be combined with a flexible-body stiffness model of choice, the engineer can determine the necessary level of detail in the stiffness analysis, as long as the resulting stiffness matrix is mapped on the end-effector Cartesian space. This flexibility is a key advantage of the presented method over other natural frequency analysis methods, which require both inertia and stiffness matrices in the same high-dimensional set of generalized coordinates.

As an example, the Heli4 robot was analyzed, for which it was shown that structural compliance has negligible influence up to an actuator stiffness of approximately 1000 Nm/rad. For higher actuator stiffness values, a model excluding structural compliance resulted in errors in the predicted natural frequencies up to 33%. It was shown that including expressions for the mechanical compliance of the links and the end-effector assembly reduced the maximum modeling error to 6%, without a need to alter the inertia analysis.

Acknowledgment

This work was supported by the Dutch Technology Foundation STW [project number 12158] and the De Breed Kreiken Innovatiefonds, which is managed by the Prins Bernhard Cultuurfonds.

Appendix A. Unit Twists and Unit Wrenches for Heli4 Robot

The analysis developed in this paper requires a set of six independent unit twists and unit wrenches for each leg. In this appendix these will be developed using the method described in Ref. [33]. The Heli4 is modeled as a 4-RRΠRR

robot because for each leg the five identified twists of permission are

$$\hat{\$}_{ta,i,1} = \begin{bmatrix} \hat{\mathbf{s}}_{i,1} \\ -\left(l_1\hat{\mathbf{r}}_{i,1} + l_2\hat{\mathbf{r}}_{i,2} - \mathbf{a}_i\right) \times \hat{\mathbf{s}}_{i,1} \end{bmatrix}$$
$$\hat{\$}_{ta,i,2} = \begin{bmatrix} \hat{\mathbf{s}}_{i,2} \\ -\left(l_2\hat{\mathbf{r}}_{i,2} - \mathbf{a}_i\right) \times \hat{\mathbf{s}}_{i,2} \end{bmatrix}$$
$$\hat{\$}_{ta,i,3} = \begin{bmatrix} \mathbf{0} \\ \hat{\mathbf{s}}_{i,3} \end{bmatrix}$$
$$\hat{\$}_{ta,i,4} = \begin{bmatrix} \hat{\mathbf{s}}_{i,4} \\ \mathbf{a}_i \times \hat{\mathbf{s}}_{i,4} \end{bmatrix}$$
$$\hat{\$}_{ta,i,5} = \begin{bmatrix} \hat{\mathbf{s}}_{i,5} \\ \mathbf{a}_i \times \hat{\mathbf{s}}_{i,5} \end{bmatrix}$$

where

$$\hat{\mathbf{s}}_{1,1} = \hat{\mathbf{s}}_{1,2} = \hat{\mathbf{s}}_{1,5} = \hat{\mathbf{e}}_2$$
$$\hat{\mathbf{s}}_{2,1} = \hat{\mathbf{s}}_{2,2} = \hat{\mathbf{s}}_{2,5} = -\hat{\mathbf{e}}_2$$
$$\hat{\mathbf{s}}_{3,1} = \hat{\mathbf{s}}_{3,2} = \hat{\mathbf{s}}_{3,5} = -\hat{\mathbf{e}}_1$$
$$\hat{\mathbf{s}}_{4,1} = \hat{\mathbf{s}}_{4,2} = \hat{\mathbf{s}}_{4,5} = \hat{\mathbf{e}}_1$$

in which $\hat{\mathbf{e}}_1$ and $\hat{\mathbf{e}}_2$ are the unit vectors aligned with the X and Y axis respectively. In addition

$$\hat{\mathbf{s}}_{1,3} = \begin{bmatrix} -\cos\left(q_{1,1} + q_{1,2}\right)\sin\left(q_{1,3}\right) \\ \cos\left(q_{1,3}\right) \\ \sin\left(q_{1,1} + q_{1,2}\right)\sin\left(q_{1,3}\right) \end{bmatrix}$$
$$\hat{\mathbf{s}}_{2,3} = \begin{bmatrix} \cos\left(q_{2,1} + q_{2,2}\right)\sin\left(q_{2,3}\right) \\ -\cos\left(q_{2,3}\right) \\ \sin\left(q_{2,1} + q_{2,2}\right)\sin\left(q_{2,3}\right) \end{bmatrix}$$
$$\hat{\mathbf{s}}_{3,3} = \begin{bmatrix} -\cos\left(q_{3,3}\right) \\ -\cos\left(q_{3,1} + q_{3,2}\right)\sin\left(q_{3,3}\right) \\ \sin\left(q_{3,1} + q_{3,2}\right)\sin\left(q_{3,3}\right) \end{bmatrix}$$
$$\hat{\mathbf{s}}_{4,3} = \begin{bmatrix} \cos\left(q_{4,3}\right) \\ \cos\left(q_{4,1} + q_{4,2}\right)\sin\left(q_{4,3}\right) \\ \sin\left(q_{4,1} + q_{4,2}\right)\sin\left(q_{4,3}\right) \end{bmatrix}$$

where $q_{i,j}$ is the value of the jth angle of the ith leg in radians, as illustrated for leg 1 in Fig. A.7. The angle $q_{i,3}$ describes the internal angle of the parallelogram. Next,

$$\hat{\mathbf{s}}_{i,4} = (\hat{\mathbf{r}}_{i,2} \times \hat{\mathbf{s}}_{i,1}) \times \hat{\mathbf{s}}_{i,1}$$

Furthermore,

$$\hat{\mathbf{r}}_{1,1} = \begin{bmatrix} \cos(q_{1,1}) \\ 0 \\ -\sin(q_{1,1}) \end{bmatrix}$$
$$\hat{\mathbf{r}}_{2,1} = \begin{bmatrix} -\cos(q_{2,1}) \\ 0 \\ -\sin(q_{2,1}) \end{bmatrix}$$
$$\hat{\mathbf{r}}_{3,1} = \begin{bmatrix} 0 \\ \cos(q_{3,1}) \\ -\sin(q_{3,1}) \end{bmatrix}$$
$$\hat{\mathbf{r}}_{4,1} = \begin{bmatrix} 0 \\ -\cos(q_{4,1}) \\ -\sin(q_{4,1}) \end{bmatrix}$$

and

$$\hat{\mathbf{r}}_{1,2} = \begin{bmatrix} \cos(q_{1,1} + q_{1,2})\cos(q_{1,3}) \\ \sin(q_{1,3}) \\ -\sin(q_{1,1} + q_{1,2})\cos(q_{1,3}) \end{bmatrix}$$
$$\hat{\mathbf{r}}_{2,2} = \begin{bmatrix} -\cos(q_{2,1} + q_{2,2})\cos(q_{2,3}) \\ -\cos(q_{2,3}) \\ \sin(q_{2,1} + q_{2,2})\sin(q_{2,3}) \end{bmatrix}$$
$$\hat{\mathbf{r}}_{3,2} = \begin{bmatrix} -\cos(q_{3,3}) \\ -\cos(q_{3,1} + q_{3,2})\sin(q_{3,3}) \\ \sin(q_{3,1} + q_{3,2})\sin(q_{3,3}) \end{bmatrix}$$
$$\hat{\mathbf{r}}_{4,2} = \begin{bmatrix} \sin(q_{4,3}) \\ -\cos(q_{4,1} + q_{4,2})\cos(q_{4,3}) \\ -\sin(q_{4,1} + q_{4,2})\cos(q_{4,3}) \end{bmatrix}$$

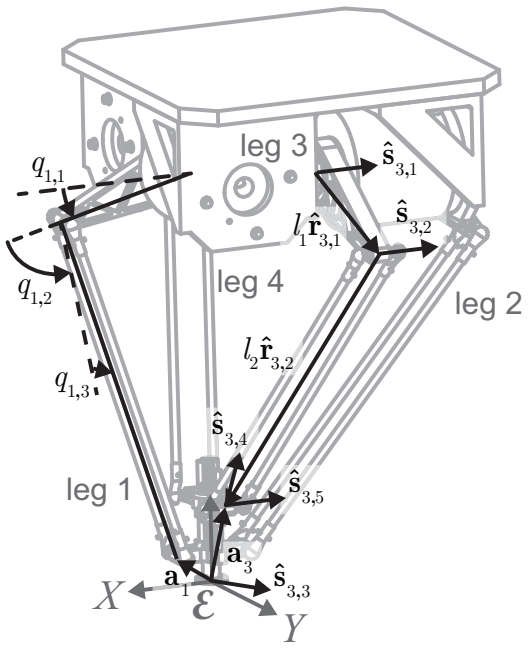

Figure A.7: Examples of the various vectors that are used in the description of the unit twists and unit wrenches of the Heli4 manipulator.

while

$$\mathbf{a}_1 = \begin{bmatrix} r \\ 0 \\ d \end{bmatrix} \quad \mathbf{a}_2 = \begin{bmatrix} -r \\ 0 \\ d \end{bmatrix}$$

$$\mathbf{a}_3 = \begin{bmatrix} 0 \\ r \\ d+h+p\theta \end{bmatrix} \quad \mathbf{a}_4 = \begin{bmatrix} 0 \\ -r \\ d+h+p\theta \end{bmatrix}$$

express the vectors from the origin of the end-effector reference frame to the connection point of the four legs, where $r = 48$ mm, $d = 78$ mm, $h = 60$ mm, $p = 9.5$ mm/rad are the parameters for the Heli4. These deviate slightly from the original parameters introduced in Ref. [35] to reflect the state of the robot during testing. Furthermore, since the end-effector assembly is considered rigid, $\theta = 0$ throughout the analysis in this paper. Figure A.7 shows examples of the various vectors introduced above.

It should be noted that the revolute joint that follows each parallelogram captures the unconstrained twisting of the two links of the parallelogram

around each other. This is the result of the use of spherical joints to connect the links of the parallelogram on either end. In the assembled parallel manipulator such twisting will not occur due to constraints imposed by the other legs. Based on the conditions described in Ref. [33], the unit wrench of constraint for each leg can be identified as

$$\hat{\$}_{wc,i,1} = \begin{bmatrix} \hat{\mathbf{r}}_{i,2} \times \hat{\mathbf{s}}_{i,1} \\ \mathbf{0} \end{bmatrix}$$

A set of wrenches of actuation can be identified as

$$\hat{\$}_{wa,i,1} = \begin{bmatrix} \mathbf{a}_i \times \hat{\mathbf{r}}_{i,2} \\ \hat{\mathbf{r}}_{i,2} \end{bmatrix}$$

$$\hat{\$}_{wa,i,2} = \frac{1}{|\mathbf{f}_{i,2}|} \begin{bmatrix} \mathbf{a}_i \times \mathbf{f}_{i,2} \\ \mathbf{f}_{i,2} \end{bmatrix}$$

$$\hat{\$}_{wa,i,3} = \begin{bmatrix} \mathbf{a}_i \times \hat{\mathbf{s}}_{i,1} \\ \hat{\mathbf{s}}_{i,1} \end{bmatrix}$$

$$\hat{\$}_{wa,i,4} = \begin{bmatrix} \hat{\mathbf{s}}_{i,4} \\ \mathbf{0} \end{bmatrix}$$

$$\hat{\$}_{wa,i,5} = \begin{bmatrix} -\left(-\sin(q_{i,3}) l_2 \hat{\mathbf{s}}_{i,2} + l_2 \hat{\mathbf{r}}_{i,2} - \mathbf{a}_i\right) \times \hat{\mathbf{f}}_{i,5} \\ \hat{\mathbf{f}}_{i,5} \end{bmatrix}$$

where

$$\mathbf{f}_{i,2} = \left((l_1 \hat{\mathbf{r}}_{i,1} + l_2 \hat{\mathbf{r}}_{i,2}) \times \hat{\mathbf{s}}_{i,1}\right) \times \hat{\mathbf{s}}_{i,3}$$

$$\mathbf{f}_{i,5} = (\hat{\mathbf{r}}_{i,1} \times \hat{\mathbf{s}}_{i,1}) \times \hat{\mathbf{s}}_{i,3}$$

Finally, the relations described in Ref. [33] allow the identification of the unit twist of restriction, namely

$$\hat{\$}_{tc,i,1} = \begin{bmatrix} \hat{\mathbf{c}}_{i,1} \\ \mathbf{a}_i \times \hat{\mathbf{c}}_{i,1} \end{bmatrix}$$

where

$$\hat{\mathbf{c}}_{i,1} = \left(\hat{\mathbf{f}}_{i,5} \times \hat{\mathbf{s}}_{i,4}\right) \times \hat{\mathbf{s}}_{i,4}$$

Appendix B. Actuator Losses

During the verification procedure it was found that the actuator torque that was generated by the actuators was lower than the commanded torque. This

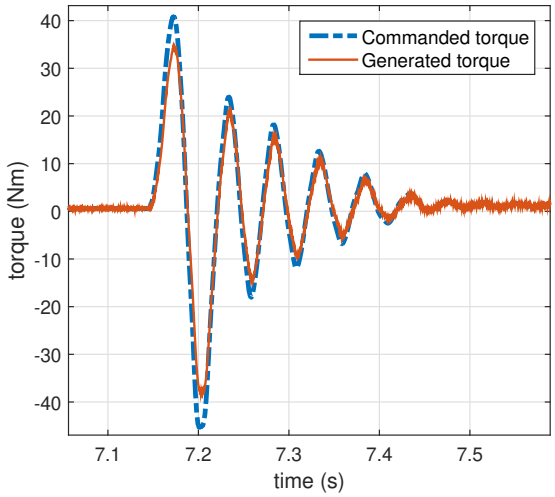

Figure B.8: It was observed during the verification tests that there was a loss a factor of 0.82 between the demanded and generated torque, here demonstrated for motor 1 with $k_a = 2000$ Nm/rad for the step input in the X-direction.

difference was consistent and described by a factor 0.82, as for example illustrated by the time trace in Fig. B.8. The data from which this time trace was generated, as well as the data recorded during other test runs is added to this paper as supplementary material. The conversion factor from ampere (A), which is a variable available in the supplementary material, to Nm is 3.65.

Appendix C. Compliance Matrix of Two Parallel, Cantilever Rods

The stiffness analysis introduced in Ref. [20] makes use of the series rule of stiffness addition to develop the compliance matrix of individual legs. According to this rule, addition of the different sources of compliance results in the total compliance of the leg. In this paper, this summation is expressed as the addition of kinematic compliance and structural compliance in the elastic joint space, as expressed in Eq. (41). The structural compliance in the elastic joint space is obtained by adding the structural compliance of all individual contributions, and subsequently projecting the total compliance matrix on the elastic joint space to 'filter out' the DoFs in which stiffness is zero.

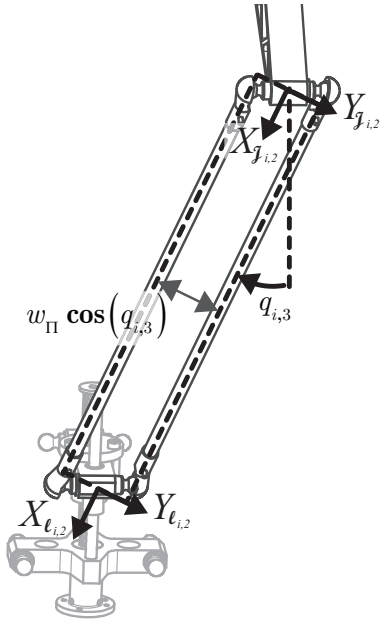

Figure C.9: To model the structural compliance of the two rods that are part of the parallelogram, they are assumed to share the rotation points located in the origins of reference frames $\mathcal{J}_{i,2}$ and $\ell_{i,2}$.

To approximate the structural compliance of the two parallel rods that make up the parallelograms, the analytically expressed stiffness matrices of the individual rods are added and subsequently inverted. The rods are considered as thick-walled cylindrical tubes with an outer radius r_o and an inner radius r_i. The structural stiffness matrix of a single rod can be obtained by taking the inverse of the symbolic compliance matrix of an Euler beam element as e.g. expressed by Eq. (24) in Ref. [40]. This results in

$$\mathbf{K}_{rod} = \begin{bmatrix} \frac{GI_x}{L} & 0 & 0 & 0 & 0 & 0 \\ 0 & \frac{4EI_y}{L} & 0 & 0 & 0 & \frac{6EI_y}{L^2} \\ 0 & 0 & \frac{4EI_z}{L} & 0 & -\frac{6EI_z}{L^2} & 0 \\ 0 & 0 & 0 & \frac{AE}{L} & 0 & 0 \\ 0 & 0 & -\frac{6EI_y}{L^2} & 0 & \frac{12EI_y}{L^3} & 0 \\ 0 & \frac{6EI_y}{L^2} & 0 & 0 & 0 & \frac{12EI_z}{L^3} \end{bmatrix} \tag{C.1}$$

where A is the cross-section area, and I_x, I_y, and I_z are the area moments of inertia for an annulus, which are expressed as

$$A = \pi \left(r_o^2 - r_i^2\right) \tag{C.2}$$

$$I_x = \frac{\pi}{2} \left(r_o^4 - r_i^4\right) \tag{C.3}$$

$$I_y = I_z = \frac{\pi}{4} \left(r_o^4 - r_i^4\right) \tag{C.4}$$

$$L = l_2 \tag{C.5}$$

In each leg of the Heli4, two of these rods are connected in parallel. The distance between the rods depends on the pose of the robot, and is defined by the angle $q_{i,3}$ as illustrated in Fig. A.7. To simplify the stiffness modeling, the two parallel rods are assumed to have the same rotation points, namely at the center of the two ends of the parallelogram. As a result, the two rods are modeled as shown in Fig. C.9. The distance between the two parallel rods is

$$d_\Pi = w_\Pi \cos(q_{i,3}) \tag{C.6}$$

As such, the structural stiffness of the two parallel rods can be expressed as

$$\mathbf{K}_{\Pi,\ell_2} = \mathbf{Ad}_{\mathbf{H}_{\ell_2}^{\Pi_1}}^\top \mathbf{K}_{rod} \mathbf{Ad}_{\mathbf{H}_{\ell_2}^{\Pi_1}} + \mathbf{Ad}_{\mathbf{H}_{\ell_2}^{\Pi_2}}^\top \mathbf{K}_{rod} \mathbf{Ad}_{\mathbf{H}_{\ell_2}^{\Pi_2}} \tag{C.7}$$

where $\mathbf{Ad}_{\mathbf{H}_{\ell_2}^{\Pi_1}}$ and $\mathbf{Ad}_{\mathbf{H}_{\ell_2}^{\Pi_2}}^\top$ are the adjoint matrices associated to the homo-

geneous matrices

$$\mathbf{H}_{\ell_2}^{\Pi_1} = \begin{bmatrix} 1 & 0 & 0 & 0 \\ 0 & 1 & 0 & \frac{d_\Pi}{2} \\ 0 & 0 & 1 & 0 \\ 0 & 0 & 0 & 1 \end{bmatrix} \tag{C.8}$$

$$\mathbf{H}_{\ell_2}^{\Pi_2} = \begin{bmatrix} 1 & 0 & 0 & 0 \\ 0 & 1 & 0 & -\frac{d_\Pi}{2} \\ 0 & 0 & 1 & 0 \\ 0 & 0 & 0 & 1 \end{bmatrix} \tag{C.9}$$

Finally, an analytical expression for structural compliance of the two parallel rods is obtained by inverting Eq. (C.7), which gives

$$\mathbf{K}_{\Pi,\ell_2}^{-1} = \begin{bmatrix} \frac{L^3}{2(GI_xL^2+3EI_yd_\Pi)} & 0 & 0 & 0 & 0 & 0 \\ 0 & \frac{L}{2EI_y} & 0 & 0 & 0 & -\frac{L^2}{4EI_y} \\ 0 & 0 & \frac{2L}{E\left(Ad_\Pi^2+4I_z\right)} & 0 & \frac{L^2}{E\left(Ad_\Pi^2+4I_z\right)} & 0 \\ 0 & 0 & 0 & \frac{L}{2AE} & 0 & 0 \\ 0 & 0 & \frac{L^2}{E\left(Ad_\Pi^2+4I_z\right)} & 0 & \frac{L^3\left(Ad_\Pi^2+16I_z\right)}{24EI_z\left(Ad_\Pi^2+4I_z\right)} & 0 \\ 0 & \frac{L^2}{4EI_y} & 0 & 0 & 0 & \frac{L^3}{6EI_y} \end{bmatrix} \tag{C.10}$$

where A, I_x, I_y, I_z, L, and d_Π where expressed in Eqs. (C.2)-(C.6) and the specific variables for Heli4 can be found in Table 1. Equation (C.10) expresses the structural compliance of the two parallel rods in a local reference frame $\ell_{i,2}$, which is indicated in Fig. C.9.

Appendix D. Compliance in End-Effector Assembly

An important source of structural compliance of the Heli4 robot is in the end-effector assembly. Most notably, compliance was observed in the kinematic coupling between the two traveling plates. A test was carried out to determine the magnitude of this compliance. The test consisted of fixing the lower traveling plate and exerting a force of 100 N on the upper traveling plate, as shown in Fig. D.10.

When the force was applied on the upper traveling along the local X-axis, the result was a rotation around the Y-axis of the lower traveling plate. The resulting displacement at the upper traveling plate was measured as 0.7 mm. This can be converted to a value for the lumped rotational stiffness as

$$k_{E,rot} = \frac{100\left(60 \cdot 10^{-3}\right)^2}{0.7 \cdot 10^{-3}} = 500 \text{ Nm/rad} \tag{D.1}$$

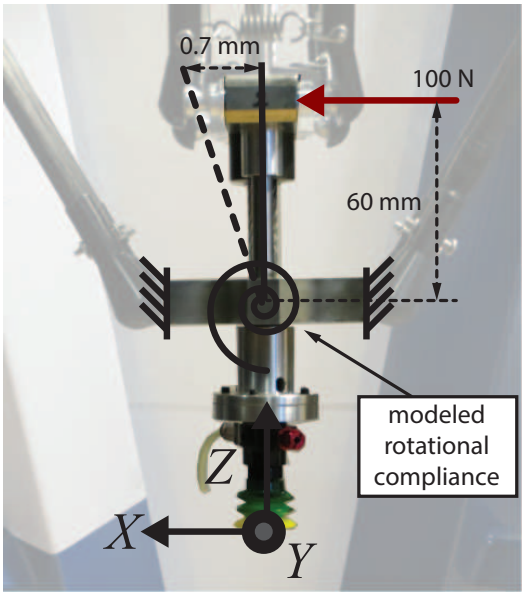

Figure D.10: One aspect of the structural compliance in the end-effector was measured using a displacement measurement under a loading of 100 N.

When the force was applied on the upper traveling along the local Y-axis, the result was a linear displacement along the Y-axis. The fact that the application of a force along the Y-axis results in a linear displacement, while application of the same force along the X-axis results in a rotational displacement, is the result of the parallelogram design of the end-effector assembly. The resulting displacement at the upper traveling plate was measured as 0.77 mm. This can be converted to a value for the lumped linear stiffness as

$$k_{E,lin} = \frac{100}{0.77 \cdot 10^{-3}} = 1.3 \cdot 10^5 \text{ N/m} \tag{D.2}$$

Appendix E. Significance of Sources of Compliance

In this paper two sources of structural compliance were included in the model, namely the rods in the parallelograms and the end-effector assembly. In this appendix the significance of both sources of compliance is discussed. First, the natural frequency analysis was repeated for the two scenarios where either the structural compliance of the end-effector assembly was removed (BM-K_E) or the structural compliance originating in the links of the parallelogram (BM-K_Π). This was simulated by dividing their compliance by a factor 1000.

Table E.3: Impact of exclusion of sources of structural compliance on the prediction error of ω_1. All values are in Hertz except the first column.

k_a [N/m]	Meas.	BM	BM - $\mathbf{K}_E^{-1}$	BM - $\mathbf{K}_\Pi^{-1}$
125	5.4	5.8	5.9	5.8
250	8.1	8.2	8.3	8.2
500	11.1	11.4	11.7	11.4
1000	15.5	15.5	16.6	15.6
1500	17.6	18.5	20.3	18.5
2000	20.3	20.7	23.5	20.7
3000	23.1	24.1	28.7	24.1
4000	25.0	26.5	33.1	26.5

Table E.4: Impact of exclusion of sources of structural compliance on the prediction error of ω_2. All values are in Hertz except the first column.

k_a [N/m]	Meas.	BM	BM - $\mathbf{K}_E^{-1}$	BM - $\mathbf{K}_\Pi^{-1}$
125	6.0	6.5	6.6	6.5
250	9.1	9.2	9.3	9.2
500	12.8	12.8	13.2	12.8
1000	18.0	17.7	18.6	17.7
1500	22.2	21.2	22.8	21.2
2000	24.0	23.9	26.3	24.0
3000	29.4	28.1	32.2	28.2
4000	31.9	31.2	37.1	31.3

The impact of exclusion of either source on the prediction error of the two lowest natural frequencies is shown in Tables E.3 and E.4.

To analyze the significance of each exclusion scenario, the measurements for ω_1 and ω_2 are combined into a single set, and the error percentages are computed according to

$$\frac{|\omega_{meas} - \omega_{pred}|}{\omega_{meas}} \cdot 100\%$$

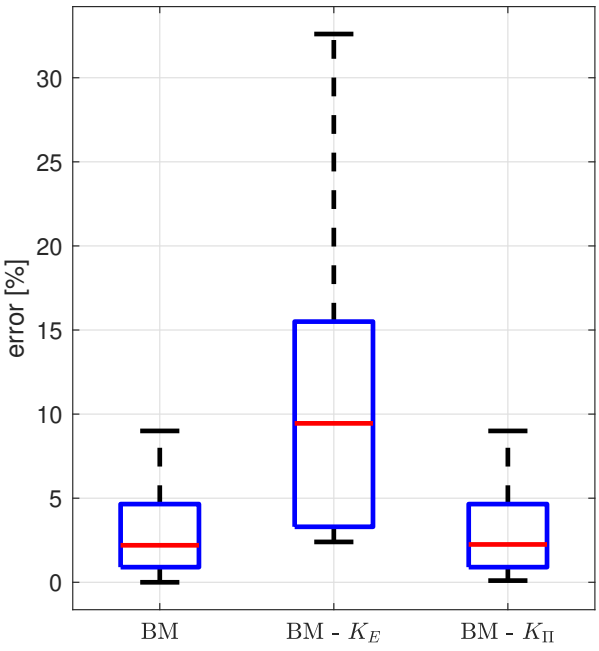

Figure E.11: Boxplots of all errors in percentages for the benchmark model (BM), BM excluding structural compliance of the end-effector assembly (BM-K_E), and BM excluding structural compliance originating in the links of the parallelogram (BM-K_Π).

where ω_{meas} are the measured natural frequencies, and ω_{pred} are the predicted natural frequencies for the considered scenario. A boxplot of the resulting values is shown in Fig. E.11.

Next, a t-test was executed in Matlab between set "BM" and sets "BM-K_E" and "BM-K_Π" respectively. The null-hypothesis that the sets "BM" and "BM-K_E" have the same mean value can be rejected at the 1% significance level, while no such conclusion can be drawn about "BM" and "BM-K_Π". Despite the limited number of measurements, it can thus be concluded that the effect of the end-effector assembly is significant, while the effect of the rods in the parallelograms is not.

References

[1] K. Bengtsson, Picking a winner and packing a punch: the second-generation FlexPicker, ABB Review 4 (2008) 29–33.

[2] B. Liao, Y. Lou, Z. Li, J. Shi, X. Chen, Design and analysis of a novel parallel manipulator for pick-and-place applications, Meccanica (aug 2015). doi:10.1007/s11012-015-0249-2.
URL http://link.springer.com/10.1007/s11012-015-0249-2

[3] F. Pierrot, V. Nabat, O. Company, S. Krut, P. Poignet, Optimal Design of a 4-DOF Parallel Manipulator: From Academia to Industry, IEEE Transactions on Robotics 25 (2) (2009) 213–224. doi:10.1109/TRO.2008.2011412.
URL http://ieeexplore.ieee.org/lpdocs/epic03/wrapper.htm?arnumber=4770157

[4] G. Wu, S. Bai, P. Hjørnet, Architecture optimization of a parallel Schönflies-motion robot for pick-and-place applications in a predefined workspace, Mechanism and Machine Theory 106 (2016) 148–165. doi:10.1016/j.mechmachtheory.2016.09.005.
URL http://dx.doi.org/10.1016/j.mechmachtheory.2016.09.005
http://linkinghub.elsevier.com/retrieve/pii/S0094114X16302075

[5] L. Birglen, C. Gosselin, N. Pouliot, B. Monsarrat, T. Laliberte, SHaDe, a new 3-DOF haptic device, IEEE Transactions on Robotics and Automation 18 (2) (2002) 166–175. doi:10.1109/TRA.2002.999645.
URL http://ieeexplore.ieee.org/lpdocs/epic03/wrapper.htm?arnumber=999645

[6] P. Lambert, J. Herder, A novel parallel haptic device with 7 degrees of freedom, in: 2015 IEEE World Haptics Conference (WHC), Vol. 31, IEEE, 2015, pp. 183–188. doi:10.1109/WHC.2015.7177711.
URL http://ieeexplore.ieee.org/lpdocs/epic03/wrapper.htm?arnumber=7177711

[7] C. Germain, S. Briot, S. Caro, P. Wenger, Natural Frequency Computation of Parallel Robots, Journal of Computational and Nonlinear Dynamics 10 (2) (2015) 021004. doi:10.1115/1.4028573.
URL http://computationalnonlinear.asmedigitalcollection.asme.org/article.aspx

[8] A. Taghvaeipour, J. Angeles, L. Lessard, Elastodynamics of a two-limb Schonflies motion generator, Proceedings of the Institution of Mechanical Engineers, Part C: Journal of Mechanical Engineering Science

229 (4) (2015) 751–764. doi:10.1177/0954406214538781.
URL http://pic.sagepub.com/lookup/doi/10.1177/0954406214538781

[9] G. Palmieri, M. Martarelli, M. C. Palpacelli, L. Carbonari, Configuration-dependent modal analysis of a Cartesian parallel kinematics manipulator: numerical modeling and experimental validation, Meccanica 49 (4) (2014) 961–972. doi:10.1007/s11012-013-9842-4.
URL http://link.springer.com/10.1007/s11012-013-9842-4

[10] L. Carbonari, Simplified approach for dynamics estimation of a minor mobility parallel robot, Mechatronics (2015) 1–9doi:10.1016/j.mechatronics.2015.06.005.
URL http://linkinghub.elsevier.com/retrieve/pii/S0957415815000896

[11] C. Gosselin, Stiffness mapping for parallel manipulators, IEEE Transactions on Robotics and Automation 6 (3) (1990) 377–382. doi:10.1109/70.56657.
URL http://ieeexplore.ieee.org/lpdocs/epic03/wrapper.htm?arnumber=56657

[12] S. Bhattacharya, D. N. Nenchev, M. Uchiyama, A recursive formula for the inverse of the inertia matrix of a parallel manipulator, Mechanism and Machine Theory 33 (7) (1998) 957–964. doi:10.1016/S0094-114X(97)00105-5.
URL http://linkinghub.elsevier.com/retrieve/pii/S0094114X97001055

[13] W. Khalil, O. Ibrahim, General Solution for the Dynamic Modeling of Parallel Robots, Journal of Intelligent and Robotic Systems 49 (2007) 19–37.
URL https://hal.archives-ouvertes.fr/hal-00401684

[14] G. Lebret, K. Liu, F. L. Lewis, Dynamic analysis and control of a stewart platform manipulator, Journal of Robotic Systems 10 (5) (1993) 629–655. doi:10.1002/rob.4620100506.
URL http://doi.wiley.com/10.1002/rob.4620100506

[15] M. Callegari, M.-C. Palpacelli, M. Principi, Dynamics modelling and control of the 3-RCC translational platform, Mechatronics 16 (10) (2006) 589–605. doi:10.1016/j.mechatronics.2006.06.001.
URL http://linkinghub.elsevier.com/retrieve/pii/S0957415806000754

[16] B. Lian, T. Sun, Y. Song, Y. Jin, M. Price, Stiffness analysis and experiment of a novel 5-DoF parallel kinematic machine considering gravitational effects, International Journal of Machine Tools and Manufacture 95 (2015) 82–96. doi:10.1016/j.ijmachtools.2015.04.012.
URL http://dx.doi.org/10.1016/j.ijmachtools.2015.04.012
http://linkinghub.elsevier.com/retrieve/pii/S0890695515300365

[17] A. Vivas, P. Poignet, F. Marquet, F. Pierrot, M. Gautier, Experimental dynamic identification of a fully parallel robot, in: IEEE International Conference on Robotics and Automation, Vol. 3, IEEE, 2003, pp. 3278–3283. doi:10.1109/ROBOT.2003.1242096.
URL http://ieeexplore.ieee.org/lpdocs/epic03/wrapper.htm?arnumber=1242096

[18] A. Cammarata, Unified formulation for the stiffness analysis of spatial mechanisms, Mechanism and Machine Theory 105 (2016) 272–284. doi:10.1016/j.mechmachtheory.2016.07.011.
URL http://dx.doi.org/10.1016/j.mechmachtheory.2016.07.011
http://linkinghub.elsevier.com/retrieve/pii/S0094114X16301446

[19] T. Detert, B. Corves, Extended Procedure for Stiffness Modeling Based on the Matrix Structure Analysis, Vol. 46 of Mechanisms and Machine Science, Springer International Publishing, Cham, 2017, pp. 299–310. doi:10.1007/978-3-319-45450-4_30.
URL http://link.springer.com/10.1007/978-3-319-45450-4
http://link.springer.com/10.1007/978-3-319-45450-4_30

[20] A. G. L. Hoevenaars, P. Lambert, J. L. Herder, Jacobian-based stiffness analysis method for parallel manipulators with non-redundant legs, Proceedings of the Institution of Mechanical Engineers, Part C: Journal of Mechanical Engineering Science 230 (3) (2016) 341–352. doi:10.1177/0954406215602283.
URL http://pic.sagepub.com/lookup/doi/10.1177/0954406215602283

[21] A. Pashkevich, D. Chablat, P. Wenger, Stiffness analysis of overconstrained parallel manipulators, Mechanism and Machine Theory 44 (5) (2009) 966–982. doi:10.1016/j.mechmachtheory.2008.05.017.
URL http://linkinghub.elsevier.com/retrieve/pii/S0094114X08001250

[22] J. Zhang, Y. Q. Zhao, M. Ceccarelli, Elastodynamic Model-Based Vibration Characteristics Prediction of a Three Prismatic-Revolute-Spherical

Parallel Kinematic Machine, Journal of Dynamic Systems, Measurement, and Control 138 (4) (2016) 041009. doi:10.1115/1.4032657.
URL http://dynamicsystems.asmedigitalcollection.asme.org/article.aspx?doi=10.

[23] A. Cammarata, On the Stiffness Analysis and Elastodynamics of Parallel Kinematic Machines, in: Serial and Parallel Robot Manipulators - Kinematics, Dynamics, Control and Optimization, no. 20, InTech, 2012. doi:10.5772/31891.
URL http://www.intechopen.com/books/serial-and-parallel-robot-manipulators-ki

[24] A. E. Firoozabadi, S. Ebrahimi, G. Amirian, Dynamic characteristics of a 3-RPR planar parallel manipulator with flexible intermediate links, Robotica (May) (2014) 1–17. doi:10.1017/S0263574714001118.
URL http://www.journals.cambridge.org/abstract_S0263574714001118

[25] K. Stachera, W. Schumacher, Derivation and Calculation of the Dynamics of Elastic Parallel Manipulators, in: Automation and Robotics, I-Tech Education and Publishing, 2008. doi:10.5772/6108.
URL http://www.intechopen.com/books/automation_and_robotics/derivation_and_cal

[26] S. Briot, W. Khalil, Recursive and symbolic calculation of the elastodynamic model of flexible parallel robots, The International Journal of Robotics Research 33 (3) (2013) 469–483. doi:10.1177/0278364913507006.
URL http://ijr.sagepub.com/cgi/doi/10.1177/0278364913507006

[27] W. Khalil, M. Gautier, Modeling of mechanical systems with lumped elasticity, in: Proceedings 2000 ICRA. Millennium Conference. IEEE International Conference on Robotics and Automation. Symposia Proceedings (Cat. No.00CH37065), Vol. 4, IEEE, 2000, pp. 3964–3969. doi:10.1109/ROBOT.2000.845349.
URL http://ieeexplore.ieee.org/document/845349/

[28] J. Yang, Z. Xu, Q. Wu, M. Zhu, S. He, C. Qin, Dynamic modeling and control of a 6-DOF micro-vibration simulator, Mechanism and Machine Theory 104 (2016) 350–369. doi:10.1016/j.mechmachtheory.2016.06.011.
URL http://dx.doi.org/10.1016/j.mechmachtheory.2016.06.011
http://linkinghub.elsevier.com/retrieve/pii/S0094114X16301161

[29] C. Alessandro, S. Rosario, Elastodynamic optimization of a 3T1R parallel manipulator, Mechanism and Machine Theory 73 (2014) 184–196. doi:10.1016/j.mechmachtheory.2013.10.010.
URL http://dx.doi.org/10.1016/j.mechmachtheory.2013.10.010
http://linkinghub.elsevier.com/retrieve/pii/S0094114X13002164

[30] B. C. Bouzgarrou, P. Ray, G. Gogu, New Approach for Dynamic Modelling of Flexible Manipulators, Proceedings of the Institution of Mechanical Engineers, Part K: Journal of Multi-body Dynamics 219 (3) (2005) 285–298. doi:10.1243/146441905X9890.
URL http://sdj.sagepub.com/lookup/10.1243/146441905X9890

[31] S. Briot, A. Pashkevich, D. Chablat, Reduced elastodynamic modelling of parallel robots for the computation of their natural frequencies, 13th World Congress in Mechanism and Machine Science (2011) 1–8.
URL http://somim.org.mx/conference_proceedings/pdfs/A12/A12_358.pdf

[32] Z. S. Chen, M. Liu, M. X. Kong, C. Ji, Modal Analysis of High-Speed Parallel Manipulator with Flexible Links, Applied Mechanics and Materials 826 (2016) 8–14. doi:10.4028/www.scientific.net/AMM.826.8.
URL http://www.scientific.net/AMM.826.8
https://www.scientific.net/AMM.826.8

[33] T. Huang, H. T. Liu, D. G. Chetwynd, Generalized Jacobian analysis of lower mobility manipulators, Mechanism and Machine Theory 46 (6) (2011) 831–844. doi:10.1016/j.mechmachtheory.2011.01.009.
URL http://linkinghub.elsevier.com/retrieve/pii/S0094114X1100019X

[34] S. a. Joshi, L.-W. Tsai, Jacobian Analysis of Limited-DOF Parallel Manipulators, Journal of Mechanical Design 124 (2) (2002) 254. doi:10.1115/1.1469549.
URL http://mechanicaldesign.asmedigitalcollection.asme.org/article.aspx?artic
http://link.aip.org/link/JMDEDB/v124/i2/p254/s1&Agg=doi

[35] S. Krut, O. Company, V. Nabat, F. Pierrot, Heli4: A parallel robot for scara motions with a very compact traveling plate and a symmetrical design, in: IEEE International Conference on Intelligent Robots and Systems, 2006, pp. 1656–1661. doi:10.1109/IROS.2006.282120.

[36] R. M. Murray, Z. Li, S. S. Sastry, A Mathematical Introduction to Robotic Manipulation, CRC Press, 1994.

[37] T. Huang, X. Zhao, D. J. Whitehouse, Stiffness estimation of a tripod-based parallel kinematic machine, IEEE Transactions on Robotics and Automation 18 (1) (2002) 50–58. doi:10.1109/70.988974.
URL http://ieeexplore.ieee.org/lpdocs/epic03/wrapper.htm?arnumber=988974

[38] T. Sun, B. Lian, Y. Song, Stiffness analysis of a 2-DoF over-constrained RPM with an articulated traveling platform, Mechanism and Machine Theory 96 (2016) 165–178. doi:10.1016/j.mechmachtheory.2015.09.008.
URL http://linkinghub.elsevier.com/retrieve/pii/S0094114X15002220

[39] J. Du, Y. Lou, Simplified dynamic model for real-time control of the delta parallel robot, in: 2016 IEEE International Conference on Information and Automation (ICIA), no. August, IEEE, 2016, pp. 1647–1652. doi:10.1109/ICInfA.2016.7832082.
URL http://ieeexplore.ieee.org/document/7832082/

[40] H. Sung Kim, H. Lipkin, Stiffness of Parallel Manipulators With Serially Connected Legs, Journal of Mechanisms and Robotics 6 (3) (2014) 031001. doi:10.1115/1.4026333.
URL http://dx.doi.org/10.1115/1.4026333